

QATAR UNIVERSITY

COLLEGE OF ARTS AND SCIENCES

VARIOGRAM MODELING FOR SPATIAL CORRELATION IN STRUCTURAL MRI

IMAGES

BY

SAED MARA'BEH

A Thesis Submitted to
the College of Arts and Sciences
in Partial Fulfillment of the Requirements for the Degree of
Masters of Science in Applied Statistics

June 2022

© 2022 Saed Mara'Beh. All Rights Reserved.

COMMITTEE PAGE

The members of the Committee approve the Thesis of
Saed Mara'Beh defended on 16/05/2022.

Dr. Esam Mahdi
Thesis/Dissertation Supervisor

Prof. Mohammad Salehi
Committee Member

Dr. Reza Pakyari
Committee Member

Approved:

Ahmed Elzatahry, Dean, College of Arts and Sciences

ABSTRACT

MARA'BEH, SAED, Masters : June : 2022, Applied Statistics

Title: Variogram Modeling for Spatial Correlation in Structural MRI Images

Supervisor of Thesis: Dr. Esam Mahdi.

In recent years neuroimaging techniques growth help us to understand the working of the human brain by using structural magnetic resonance imaging (sMRI) and functional magnetic resonance imaging (fMRI). Structural MRIs are used to show the main structure of the brain organism such as gray matter, white matter, and cerebrospinal fluid (CSF). The functional MRI is used to study the brain activity when performing an assigned task like eyes moving and talking. It uses the bloodoxygen- level dependent (BOLD) contrast, when there is an activity in a region of the brain the blood flow to that area will increase. In this research, geostatistical techniques such as the variogram and kriging approaches are utilized to uncover the spatial correlation in structural magnetic resonance imaging (sMRI) data and to predict the effect of a brain tumor on brain regions. We propose different variogram models approach for three brain slices containing a brain tumor and we find that the best models for slices 10 and 11 is the exponential model and for slice 12 is the Gaussian model, the best model is selected by using the cross - validation method in kriging. A bootstrap resampling method is used to estimate the empirical variogram values and the parameters of the selected models.

DEDICATION

*To my wife, **Haneen**, I would not be who I am without your support and love.*

*To my daughters, **Sereen** and **Ayla**, study hard because the feeling of success is the
best thing in the entire world.*

ACKNOWLEDGMENTS

First I would like to express my gratitude to my supervisor Dr. Esam Mahdi for the useful comments, remarks and engagement through the learning process of this master thesis. Besides my advisor, I would like to thank the rest of my thesis committee: Prof. Mohammad Salehi, Dr. Riza Pakyari, Prof. Mohammad Nasser from Qatar University and Prof. Yuhlong Lio from University of South Dakota for their encouragement and insightful comments. All thanks go to Qatar University and particularly Department of Mathematics, Statistics and Physics for providing sufficient study and research environment. I thank all those who taught me in the graduate study. Last, but by no means least, my thanks to my beloved family, parents, my brothers and the rest of my relatives and friends for their prayers and support.

Contents

DEDICATION	iv
ACKNOWLEDGMENTS	v
LIST OF TABLES	viii
LIST OF FIGURES	ix
Chapter 1: Introduction	1
Chapter 2: The variogram	7
2.1 The concept of variogram	7
2.2 Variogram parameters	8
2.3 Variogram modelling	11
2.4 Fitting variogram model	18
2.5 Kriging	19
Chapter 3: Variogram modelling for structural MRI data	24
3.1 Data Description	24
3.1.1 Image format	24
3.1.2 Masking the brain	26
3.2 Variogram modelling	29
3.2.1 Validation of Stationary assumption	31
3.2.2 Validation of Isotropy Assumption	37
3.2.3 Model selection	40
3.3 Bootstrap sampling for estimating variogram parameters	45
Chapter 4: Conclusion and future work	54

References	55
Appendix A: Histogram of the estimated parameters	60
Appendix B: Fitted models to the directional empirical models	63
Appendix C: Empirical Variogram of all slices	70

LIST OF TABLES

Table 3.1 Number of voxels for the tumor region in the slices 10, 11 and 12	27
Table 3.2 A matrix of numbers correspond to 195 to 210 voxel in the x direction and 130 to 140 voxel in the y direction of the brain slice in figure 3.2a	27
Table 3.3 MSDR of the variogram models approach in 3.12	43
Table 3.4 MSDR of the variogram models approach in 3.13	43
Table 3.5 MSDR of the variogram models approach in 3.14	43
Table 3.6 MSDR of variogram models approach in figures 3, 4 and 5	44
Table 3.7 MSDR of variogram models approach in figures 6, 7 and 8	44
Table 3.8 MSDR of variogram models approach in figures 9, 10 and 11	44
Table 3.9 The estimated parameters for the fitted directional variogram models in tables 3.6, 3.7 and 3.8	45
Table 3.10 Original Variogram	46
Table 3.11 95% confidence interval for the variogram parameters estimated by the cloud bootstrap method	48
Table 3.12 95% confidence interval for the variogram parameters estimated by the variogram bootstrap method.	48

LIST OF FIGURES

Figure 1.1 Proton spinning movement	2
Figure 1.2 Protons spinning in random directions with net magnetization equal to zero	2
Figure 1.3 A longitudinal magnetization in the direction of the field	3
Figure 2.1 Variogram Parameters	9
Figure 2.2 Variogram of Magnesium concentration in the soil of Walker Lake, lag spacing = 5.....	9
Figure 2.3 Anisotropy semivariogram of Magnesium concentration in the soil of Walker Lake.....	10
Figure 2.4 Bounded linear variogram model	11
Figure 2.5 Unbounded linear variogram model	12
Figure 2.6 Circular variogram model	13
Figure 2.7 Spherical variogram model	13
Figure 2.8 Pentaspherical variogram model	14
Figure 2.9 Exponential variogram model	15
Figure 2.10 Gaussian variogram model	16
Figure 2.11 Pure nugget model	17
Figure 3.1 22 axial slice image of the brain, the slices starts from the bottom to top of the head	25
Figure 3.2 DICOM images of the 11th and 12th slice of the brain with dimension 288 × 288 pixel.	25
Figure 3.3 Panels (a), (c) and (c) represent the ROI images of the 10th, 11th and 12th slice of the brain respectively and panels (b), (d), (f) are plots ROI images as spatial	

data	28
Figure 3.4 Panels (a) and (c) show the variogram cloud for the image data in slices 10 and 11 respectively while panels (b) and (d) show the empirical variogram of these data.	30
Figure 3.4 Panel (e) shows the variogram cloud for the image data in slice 12 while panel (f) shows the empirical variogram of this data.	31
Figure 3.5 Panels (a), (c), and (e) are local variograms for the corresponding randomly selected points of slice 10 in panels (b), (d), and (f). The numbers of selected points in panels (b), (d), and (f) are 200, 500, and 800 respectively	32
Figure 3.5 Panel (g) and (i) are the local variograms for the corresponding randomly selected points of slice 10 in panels (h) and (j). The numbers of selected points in panels (h) and (j) are 1200 and 1500 respectively.	33
Figure 3.6 Panels (a) is local variograms for the corresponding randomly selected points of slice 11 in panel (b). The number of selected points in panel (b) is 200	33
Figure 3.6 Panel (c), (e) and (g) are the local variograms for the corresponding randomly selected points of slice 11 in panels (d), (f), and (h). The number of selected points in panels (h) and (j) are 500, 800, and 1200 respectively.	34
Figure 3.6 Panel (i) is the local variogram for the corresponding randomly selected points of slice 11 in panel (j). The number of selected points in panel (j) is 1200.	35
Figure 3.7 Panels (a) is local variograms for the corresponding randomly selected points of slice 12 in panel (b). The number of selected points in panel (b) is 200.....	35
Figure 3.7 Panel (c), (e), and (g) are the local variograms for the corresponding randomly selected points of slice 12 in panels (d), (f), and (h). The number of selected points in panels (d), (f), and (h) are 400, 600, and 800.....	36
Figure 3.8 Rose diagram of the empirical variogram for data in slice 10	37

Figure 3.9 Rose diagram of the empirical variogram for data in slice 11 38

Figure 3.10 Rose diagram of the empirical variogram for data in slice 12 38

Figure 3.11 Panels (a) - (c) shows directional variogram for data of slice 10, panels (d) - (f) shows directional variogram for data of slice 11, and panels (g) - (i) shows directional variogram for data of slice 12 39

Figure 3.12 Exponential, spherical, Gaussian, and circular models are fitted (solid line) to the empirical variograms (dotted line) in Fig. 3.4b40

Figure 3.13 Exponential, spherical, Gaussian, and circular models are fitted (solid line) to the empirical variograms (dotted line) in Fig. 3.4d 41

Figure 3.14 Exponential, spherical models are fitted (solid line) to the empirical variograms (dotted line) in Fig. 3.4f 41

Figure 3.14 Gaussian, and circular models are fitted (solid line) to the empirical variograms (dotted line) in Fig. 3.4f 42

Figure 3.15 Panels (a), (c), and (d) show the original variogram and the variogram of each bootstrap performed by variogram bootstrap for the slices 10, 11, and 12 respectively. Panels (b), (d), and (f) are the original Variogram and the variogram of each bootstrap based on variogram cloud.47

Figure 3.16 Panels (a) and (c) shows the original sill and estimated sill values for each bootstrap by using bootstrap of the variogram cloud while panels (b) and (d) are from bootstrap based on error from the fitted model of the variogram. (- original sill, - confidence interval bounds, • average of sill bootstrap values).50

Figure 3.16 Panels (e) and (f) shows the original sill and estimated sill values for each bootstrap by using bootstrap of the variogram cloud and bootstrap based on error from the fitted model of the variogram respectively. (- original sill, - confidence interval bounds, • average of sill bootstrap values)51

Figure 3.17 Panels (a) and (c) shows the original nugget and estimated nugget values for each bootstrap by using bootstrap of the variogram cloud while panels (b) and (d) are from bootstrap based on error from the fitted model of the variogram. (- original nugget, - confidence interval bounds, • average of nugget bootstrap values)52

Figure 3.17 Panels (e) and (f) shows the original nugget and estimated nugget values for each bootstrap by using bootstrap of the variogram cloud and bootstrap based on error from the fitted model of the Variogram respectively. (- original nugget, - confidence interval bounds, • average of nugget bootstrap values)53

Figure 1 Panels (a) and (c) show a histogram of bootstrap sill values by using the bootstrap of the variogram cloud, while panels (b) and (d) are from bootstrap based on error from the fitted model of the Variogram (- original sill, - confidence interval bounds, • average of sill bootstrap values) 60

Figure 1 Panel (e) shows a histogram of bootstrap sill values by using the bootstrap of the variogram cloud, while panel (f) are from bootstrap based on error from the fitted model of the variogram (- original sill, - confidence interval bounds, • average of sill bootstrap values) 61

Figure 2 Panel (a) shows a histogram of bootstrap nugget values by using the bootstrap of the variogram cloud, while panel (b) are from bootstrap based on error from the fitted model of the variogram (- original nugget, - confidence interval bounds, • average of nugget bootstrap values) 61

Figure 2 Panels (c) and (e) show a histogram of bootstrap nugget values by using the bootstrap of the variogram cloud, while panels (f) and (d) are from bootstrap based on error from the fitted model of the Variogram (- original nugget, - confidence interval bounds, • average of nugget bootstrap values) 61

Figure 3 Exponential, Gaussian, circular, and spherical models are fitted (solid line) to

the empirical variograms (dotted line) in Fig. 3.11a	63
Figure 4 Exponential, Gaussian, circular, and spherical models are fitted (solid line) to the empirical variograms (dotted line) in Fig. 3.11b	63
Figure 5 Exponential and Gaussian models are fitted (solid line) to the empirical variograms (dotted line) in Fig. 3.11c	64
Figure 5 Circular and spherical models are fitted (solid line) to the empirical variograms (dotted line) in Fig. 3.11c	65
Figure 6 Exponential, Gaussian, circular, and spherical models are fitted (solid line) to the empirical variograms (dotted line) in Fig. 3.11d	65
Figure 7 Exponential, Gaussian, circular, and spherical models are fitted (solid line) to the empirical variograms (dotted line) in Fig. 3.11e	66
Figure 8 Exponential and Gaussian models are fitted (solid line) to the empirical variograms (dotted line) in Fig. 3.11f	66
Figure 8 Circular and spherical models are fitted (solid line) to the empirical variograms (dotted line) in Fig. 3.11f	67
Figure 9 Exponential, Gaussian, circular, and spherical models are fitted (solid line) to the empirical variograms (dotted line) in Fig. 3.11g	67
Figure 10 Exponential, Gaussian, circular, and spherical models are fitted (solid line) to the empirical variograms (dotted line) in Fig. 3.11h	68
Figure 11 Exponential and Gaussian models are fitted (solid line) to the empirical variograms (dotted line) in Fig. 3.11c	68
Figure 11 Circular and spherical models are fitted (solid line) to the empirical variograms (dotted line) in Fig. 3.11c	69
Figure 12 Panels (a), (c) and (e) show the MRI images for slices 7, 8 and 9 in figure 3.1 and panels (b), (d) and (f) represent the region of interest for these slices	

respectively.....70

Figure 13 3 dimension plot for the data in slices 7,8,9,10,11 and 1271

Figure 14 Empirical variogram for the data in slices 7, 8, 9, 10, 11, and 12 71

Table 3.1 Number of voxels for the tumor region in the slices 10, 11 and 12	27
Table 3.2 A matrix of numbers correspond to 195 to 210 voxel in the x direction and 130 to 140 voxel in the y direction of the brain slice in figure 3.2a	27
Table 3.3 MSDR of the variogram models approach in 3.12	43
Table 3.4 MSDR of the variogram models approach in 3.13	43
Table 3.5 MSDR of the variogram models approach in 3.14	43
Table 3.6 MSDR of variogram models approach in figures 3, 4 and 5	44
Table 3.7 MSDR of variogram models approach in figures 6, 7 and 8	44
Table 3.8 MSDR of variogram models approach in figures 9, 10 and 11	44
Table 3.9 The estimated parameters for the fitted directional variogram models in tables 3.6, 3.7 and 3.8	45
Table 3.10 Original Variogram	46
Table 3.11 95% confidence interval for the variogram parameters estimated by the cloud bootstrap method	48
Table 3.12 95% confidence interval for the variogram parameters estimated by the variogram bootstrap method.	48

CHAPTER 1: INTRODUCTION

The current research studies in medical sciences involve data that are randomly collected during the time over specified locations ([14], [22], [28], [31], [33] [38]). The variogram models are the most commonly method used to describe the spatial continuity of the data. These models measure the variability between pairs of two points at various distances. The variogram models are used to describe the statistical characters of adjacent points in images, in medical field we apply this technique on Magnetic Resonance Imaging (MRI).

Magnetic Resonance Imaging (MRI) is a radiological technique that is used to form images of the body. It can be used to study both brain structure, and brain function [29]. The structural MRIs are used to show the main structure of the brain as gray matter, white matter and cerebrospinal fluid (CSF). The radiologist uses these images to inspect pathological lesions or anatomical deformities. The functional MRI is used to study brain activity when performing an assigned task like eyes moving and talking. It uses the blood-oxygen-level dependent (BOLD) contrast, when there is an activity in a region of the brain the blood flow to that area will increase ([6], [21]). Up to 60% of the human body is water (H_2O) so the hydrogen atoms, which consist of a single proton, are abundant in human organisms. Protons can be viewed as positively charged spheres that are always spinning (see Fig. 1.1).



Figure 1.1: Proton spinning movement

The net magnetization of all nuclei are measured, it can be viewed as vector of two components [18], the longitudinal component parallel to the magnetic field and the transverse component perpendicular to the field. In the absence of an external magnetic field, the nuclear magnetic moments are randomly oriented. Therefore, the net magnetization is zero (see Fig. 1.2).

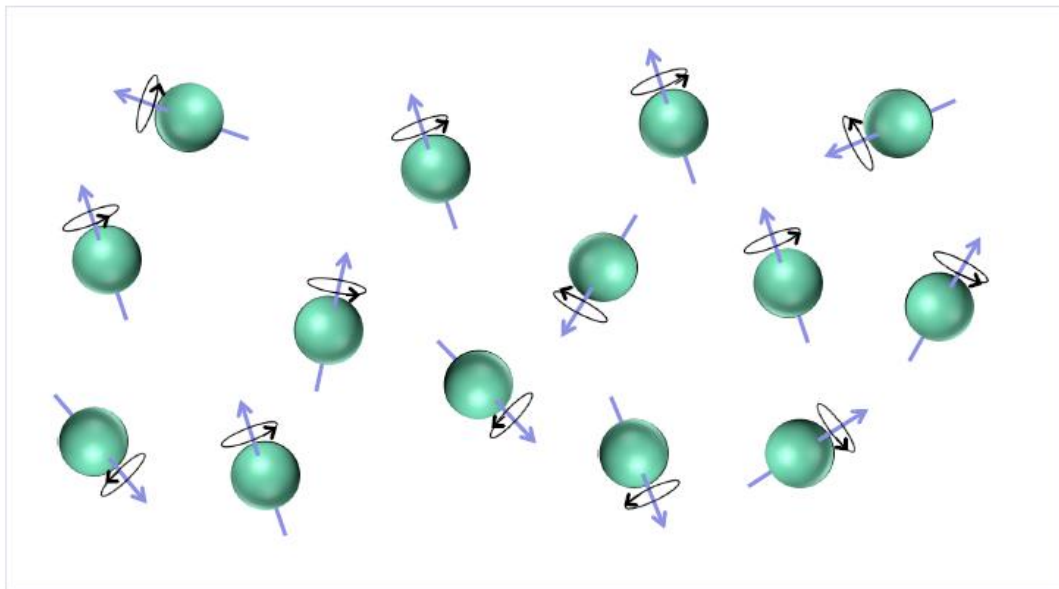


Figure 1.2: Protons spinning in random directions with net magnetization equal to zero

When we placed a human body in the MRI scanner with a strong magnetic field, the nuclei stratify with the field and this will create a net longitudinal magnetization in the direction of the field as shown in Fig. 1.3 [21].

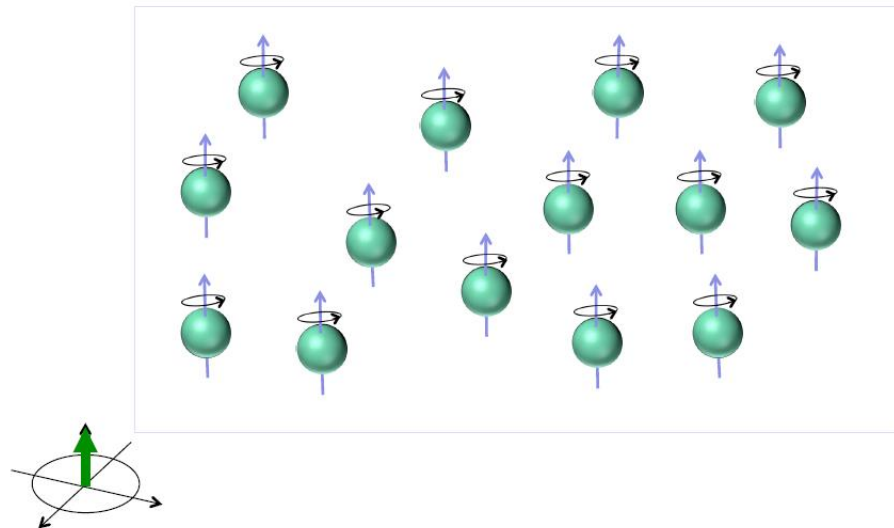


Figure 1.3: A longitudinal magnetization in the direction of the field

The nuclei precess about the field with an angular frequency determined by the *Larmor frequency* but at a random phase. A radio frequency (RF) vibration is used to range the phase and ‘tip over’ the nuclei. This causes the longitudinal magnetization to decrease, and establishes a new transversal magnetization [6].

After the RF vibration is removed the transverse magnetization starts to disappear and the longitudinal magnetization grows back to its original size. During this process, a signal is created that can be measured using a receiver coil, from this signal a MRI image is constructed or a matrix of numbers that correspond to spatial locations.

There are many researches and literature review about the application of variogram and kriging in MRI images and data. Katanoda, Matsuda, and Sugishita

(2002) used the generalized least squares method (GLS) instead of ordinary least squares (OLS) to find a spatio-temporal regression for detecting the active regions in the fMRI data. This model take account the spatial autocorrelation between the neighborhood voxels in finding the model formula and estimating the parameters [23].

Feng Gui and Lin Qi Wei (2004) proposed a variogram model of MRI data based on image segmentation, which is separating the image into several regions regarding to its texture properties. They used the value of the variogram model to describe the statistical characters of adjacent locations (points) in the the MR image, which implied that different textures have different variogram values [15].

F Dubois Bowman (2007) presented spatiotemporal models based on a metric distance that shows the relations between voxels based on functional relations than anatomic relations. These functional relations between voxels measures the similarity in brain activity accurately than physical distances [5].

Xian-Chuan Yu, Xiao-Chun Cheng, Chen Yu, Dig Zhang and Shao-Chun Zhnog (2004) used factorial kriging, which is a kriging analysis for a nested combination of two or more variogram models. By factorial analysis they recognized the active areas in fMRI of auditory stimulation tested data [40].

Brandon Whitcher, Volker J. Schmid and Andrew Thornton (2011) developed two packages in R for interacting and manipulating medical imaging data that conform to NIFTI (Neuroimaging Informatics Technology Initiative) or DICOM (Digital Inaging and Communications in Medicine) format, the **oro.nifti** and **oro.dicom** packages. From these two packages we can read and visualize the functional and structural MRI data ([37] *and* [38]).

Ye, Lazar and Li (2015) proposed a parametric variogram model which is the Gaussian model with sill values 1, 1.5 and 2 and a nonparametric variogram model

which merged between the Gaussian model and the Bessel variogram model. The proposed function considered the physical and functional relations in the brain voxels (volumetric pixel) [39].

Wenjie, Haipeng and Young (2016) discussed the strengths and the weaknesses of commonly statistical methods used for analysis of fMRI data. They proposed a spatio-temporal model that is used for localizing dynamic processes (such as neuronal activity) in the brain [7].

Marschallinger, R., Tur, C., Marschallinger, H., and Sellner, J. (2021) presented a script that generates the Multiple Sclerosis - Lesion Pattern Discrimination (MS-LDP) Plot and variogram plots by using the R package *LDPgenerator.r*. The data is three phantoms of brains with MS-lesions in Nifti format files with a binary MS-WML mask (voxel value is 1 for the region of interest and 0 otherwise). The fitted model was the exponential model to the three directional variograms x , y and z . The MS-LDP parameters are combining the range and the sill values of the three directional variograms by their means [27].

Dong, T., Huang, Q., Huang, S., Xin, J., Jia, Q., Gao, Y., Shen, H., Tang, Y., and Zhang, H. (2021) tested the correlation of brain activity on Methamphetamine (MA) abstainers. They took a resting-state functional magnetic resonance imaging (RS-fMRI) scan for 47 detoxed people and 44 normal people (control group). The authors perform data analysis by using machine learning techniques such as independent component analysis (ICA), decision tree, k-means clustering and sliding window technique. The results have shown that there is differences in brain network parts of MA abstainers from normal people [10].

In this work we will discuss in chapter 2 the concept of variogram (section 2.1), variogram parameter (section 2.2), variogram modeling (section 2.3), fitting variogram

(section 2.4), and kriging technique (section 2.5). In chapter 3 we will discuss the variogram modeling for structural MRI data. First we read the data from the three slices of MRI image contain a brain tumor, this can be done by using the brain mask process (subsection 3.1.2). Then we calculate the empirical variogram for the selected slices and we use the K -fold cross validation to choose the best model (section 3.2). In section 3.3 we use the bootstrap sampling technique to estimate the variogram values and variogram parameters and in chapter 4 we discuss some future work.

CHAPTER 2: THE VARIOGRAM

2.1 The concept of variogram

The history of variogram is associated with the field of gold mining. It gives a measure of how much two samples taken from the mining area will vary in gold percentage depending on the distance between those samples. Samples taken far apart will vary more than samples taken close to each other [24].

let $\{Z(s_i)\}$ be the values at locations $s_i, i = 1, 2, \dots, n$. The general spatial model is given by ([21], [25])

$$Z(s) = \mu + \varepsilon(s), \quad (2.1)$$

where μ is a constant population mean and $\varepsilon(s)$ is a random error with mean zero. $Z(s)$ is second order stationary if it satisfies the following two conditions:

- $E(Z(s_i)) = E(Z(s_i + h)) = \mu$
- $\text{cov}(Z(s_i + h), Z(s_i)) = C(h)$,

where lag h is the separation distance in the specified direction between two locations $s_i + h$ and s_i . The value of the variogram is defined by [21]

$$2\gamma(h) = \text{Var}(Z(s_i + h) - Z(s_i)) \quad (2.2)$$

which implies that

$$2\gamma(h) = \text{Var}(Z(s_i + h) - Z(s_i)) = E(((Z(s_i + h) - \mu(s_i + h)) - (Z(s_i) - \mu(s_i)))^2) \quad (2.3)$$

Since the mean is constant then Eq. (2.3) will be equivalent to

$$2\gamma(h) = E((Z(s_i + h) - Z(s_i))^2) = 2C(0) - 2C(h),$$

Therefore,

$$\gamma(h) = C(0) - C(h), \quad (2.4)$$

where $\gamma(h)$ is called the **semivariogram** [35].

The empirical semivariogram $\hat{\gamma}(h)$ is calculated by

$$\hat{\gamma}(h) = \frac{1}{2N(h)} \sum_{i=1}^{N(h)} (Z(s_i + h) - Z(s_i))^2, \quad (2.5)$$

Where $N(h)$ is the number of pairs of samples with a distance of h from each other. $Z(s_i + h)$ and $Z(s_i)$ are the sample values at locations $s_i + h$ and s_i respectively.

Properties:

- $\gamma(s_i, s_j) = \frac{1}{2N(h)} \sum_{i=1}^{N(h)} (Z(s_i) - Z(s_j))^2 \geq 0$, for any two locations s_i and s_j , where $h = |s_i - s_j|$.
- The semivariogram at distance zero is zero, $\gamma(s_i, s_i) = 0$.
- The semivariogram is symmetric, i.e $\gamma(s_i, s_j) = \gamma(s_j, s_i)$ for any two locations s_i and s_j .
- The semivariogram is a conditionally negative definite function [18]; that is for weights w_1, w_2, \dots, w_n such that $\sum_{i=1}^n w_i = 0$ and locations s_1, s_2, \dots, s_n

$$\sum_{i=1}^n \sum_{j=1}^n w_i \gamma(s_j, s_i) w_j \leq 0. \quad (2.6)$$

- The semivariogram is an even function, i.e. $\gamma(h) = \gamma(-h)$.

2.2 Variogram parameters

As the separation distance between two locations increases the value of the variogram will also increase. However, as the separation distance increase, the variogram reaches the stage of stability which is called the **sill** c_0 . The distance at which the variogram reaches the stability is called the **range** a_0 . The value of the variogram at lag $h = 0$ is 0, however, for several factors such as sampling error the value of the variogram at lag $h = 0$ may not be equal to 0 and this causes a discontinuity at the origin of the variogram graph. The difference between the value 0 at the origin and the value of the variogram at the extremely small lag is called the **nugget effect** c_n , see Fig.

2.1 [4].

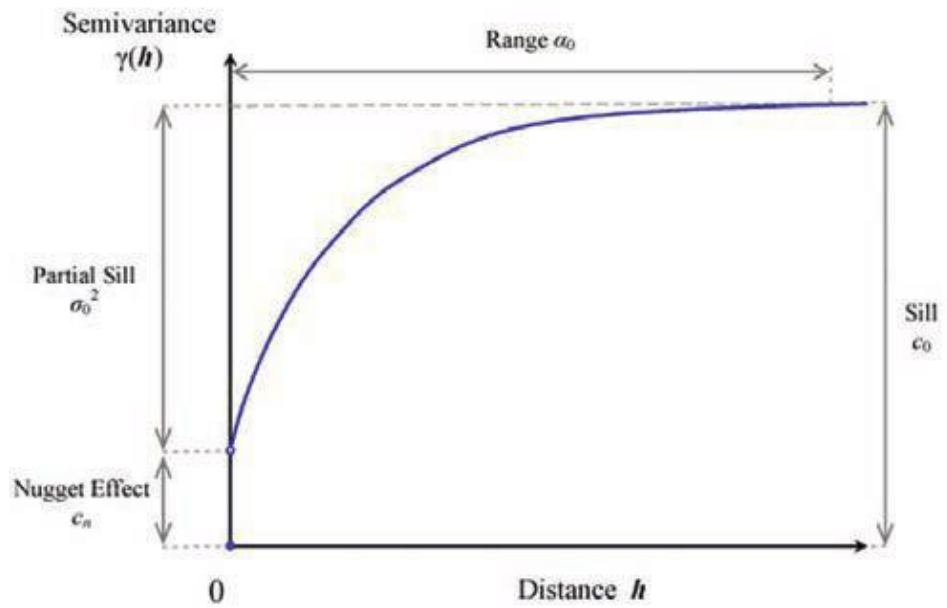


Figure 2.1: Variogram Parameters

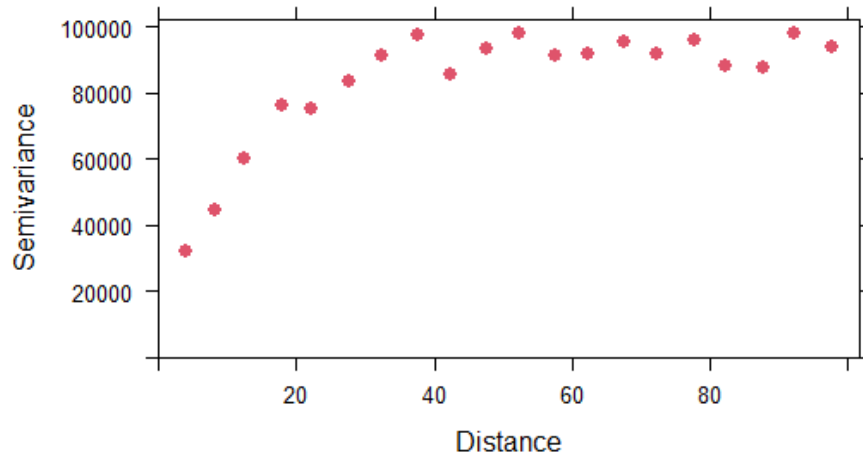


Figure 2.2: Variogram of Magnesium concentration in the soil of Walker Lake, lag spacing = 5

Eq. (2.5) shows how the values $Z(s_i)$ depend on the relative orientation of data

locations $s_i, i = 1, 2, \dots, n$. If the semivariogram depends on only the (Euclidean) distance between locations, then the semivariogram is **isotropic**. Fig 2.2 shows an isotropic variogram for the magnesium concentration in the soil of Walker Lake. However, if the semivariogram depends not on only the distance but also on the direction then we have **an anisotropic** semivariogram, as shown in Fig 2.3 semivariograms of Magnesium concentration in the soil of Walker Lake in different directions. There are two types of an anisotropy, *geometric* and *zonal* anisotropy. Geometric anisotropy exists when the range of the semivariogram changes with directions. Zonal anisotropy occurs when the sill and the range of the semivariogram changes in a different direction [21].

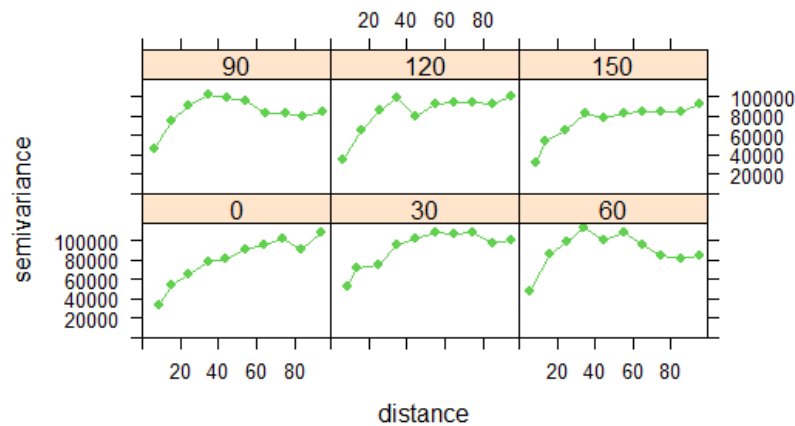


Figure 2.3: Anisotropy semivariogram of Magnesium concentration in the soil of Walker Lake.

2.3 Variogram modelling

The variograms have different models, most of these models have maximum variance known as a *sill*. The variogram may reach its sill at a finite lag distance called the *range*. The variogram may approach its sill asymptotically or in some models fluctuate about it. Here are the most popular variogram models [36].

- **Linear Model.**

There are two types of linear models, bounded and unbounded models. The bounded variogram model is defined by

$$\gamma(h) = \begin{cases} c_0 + c \left(\frac{h}{a}\right), & \text{for } 0 < h \leq a \\ c_0 + c, & \text{for } h > a \\ 0, & \text{for } h = 0 \end{cases} \quad (2.7)$$

where c_0 is the nugget, $c_0 + c$ is the sill, and a is the range. The function $\gamma(h)$ tend to $c_0 + c$ as $h \rightarrow \infty$. This model is valid in one dimension (see Fig. 2.4).

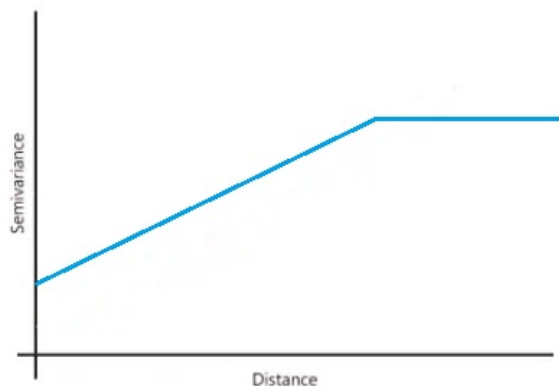


Figure 2.4: Bounded linear variogram model

The unbounded variogram models is defined by

$$\gamma(h) = \begin{cases} c_0, & \text{for } h = 0 \\ c_0 + ch, & \text{for } h > 0 \end{cases} \quad (2.8)$$

where c_0 is the nugget and the function $\gamma(h)$ tend to ∞ as $h \rightarrow \infty$ and it is valid in \mathbb{R}^d for $d \geq 1$ (see Fig. 2.5).

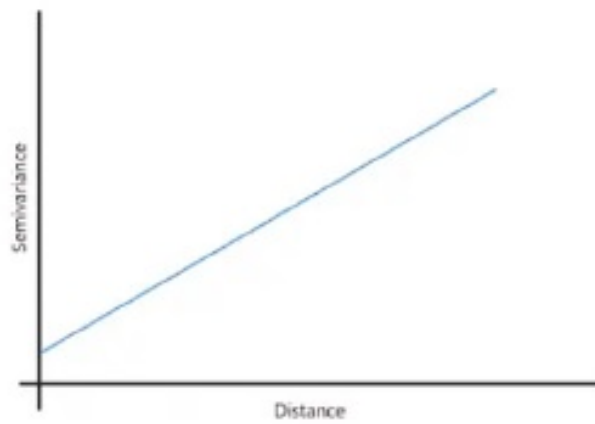


Figure 2.5: Unbounded linear variogram model

• **Circular Model.** The formula of the circle variogram is given by

$$\gamma(h) = \begin{cases} c_0 + c \left(1 - \frac{2}{\pi} \cos^{-1}\left(\frac{h}{a}\right) + \frac{2h}{\pi a} \sqrt{1 - \frac{h^2}{a^2}} \right), & \text{for } 0 < h \leq a \\ c_0 + c, & \text{for } h > a \\ 0, & \text{for } h = 0 \end{cases} \quad (2.9)$$

where the nugget, the sill and the range denoted c_0 , $c_0 + c$ and a respectively. It is valid for one and two dimensions (see Fig. 2.6).

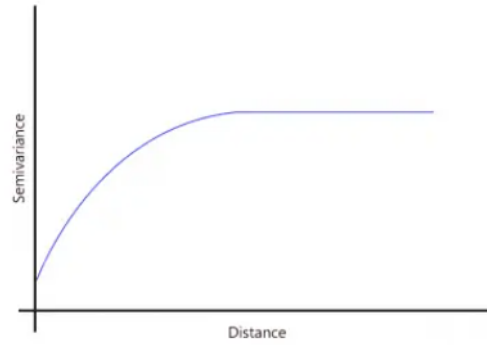


Figure 2.6: Circular variogram model

• **Spherical Model**

$$\gamma(h) = \begin{cases} c_0 + c \left\{ \frac{3h}{2a} - \frac{1}{2} \left(\frac{h}{a} \right)^3 \right\}, & \text{for } 0 < h \leq a, \\ c_0 + c, & \text{for } h > a \\ 0 & \text{for } h = 0 \end{cases} \quad (2.10)$$

where c_0 is the nugget, $c_0 + c$ is the sill and a is the range. This model is valid for one, two and three dimensions (see Fig. 2.7).

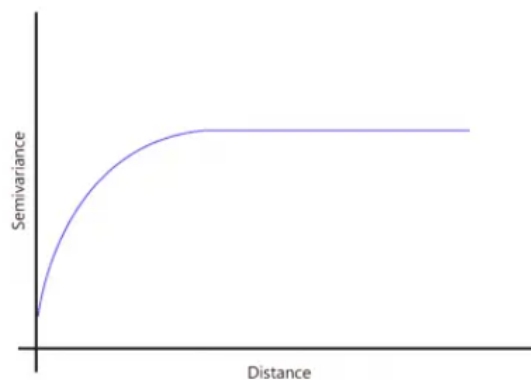


Figure 2.7: Spherical variogram model

• **Pentaspherical Model**

$$\gamma(h) = \begin{cases} c_0 + c \left\{ \frac{15h}{8a} - \frac{5}{4} \left(\frac{h}{a} \right)^3 + \frac{3}{8} \left(\frac{h}{a} \right)^5 \right\} & \text{for } 0 < h \leq a \\ c_0 + c & \text{for } h > a \\ c_0 & \text{for } h = 0 \end{cases} \quad (2.11)$$

where c_0 is the nugget, $c_0 + c$ is the sill and a is the range and it is valid in \mathbb{R}^d for $d = 1, 2$ and 3 (see Fig. 2.8).



Figure 2.8: Pentaspherical variogram model

• **Exponential Model**

$$\gamma(h) = \begin{cases} c_0 + c \left\{ 1 - e^{-\frac{h}{a}} \right\}, & \text{for } h > 0. \\ c_0, & \text{for } h = 0 \end{cases} \quad (2.12)$$

This model is valid in \mathbb{R}^d for $d \geq 1$. The sill of this model is $c_0 + c$ and the nugget is c_0 . The distance parameter a defines the spatial extent of the model. This model without a finite range since it approaches its sill asymptotically (see Fig. 2.9).

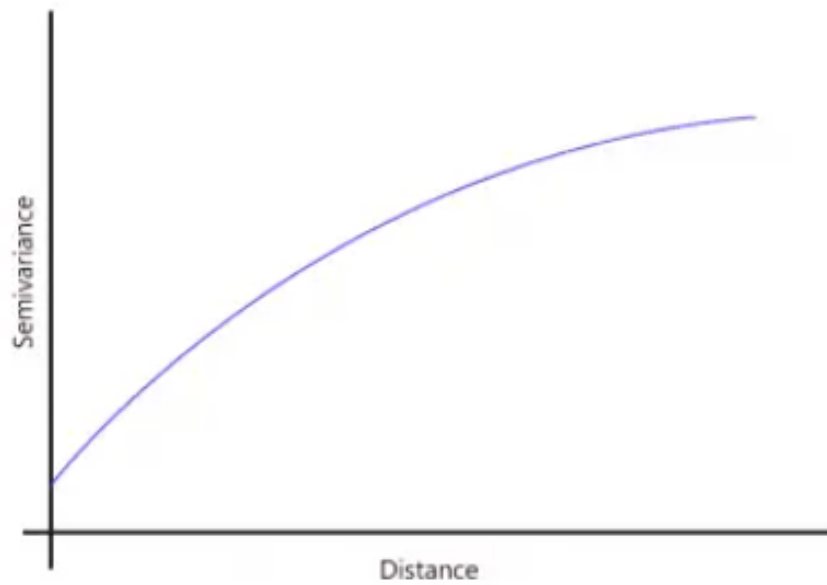


Figure 2.9: Exponential variogram model

- **Gaussian model**

This model is valid in any dimension and it is given by

$$\gamma(h) = \begin{cases} c_0 + c \left(1 - e^{-\left(\frac{h}{a}\right)^2} \right), & \text{for } h > 0 \\ c_0, & \text{for } h = 0 \end{cases} \quad (2.13)$$

similar to exponential model, c_0 is the nugget, $c_0 + c$ is the sill and a is the distance parameter. The model approaches its sill asymptotically and it has a finite effective range which is approximately $\sqrt{3}a$ (see Fig. 2.10).

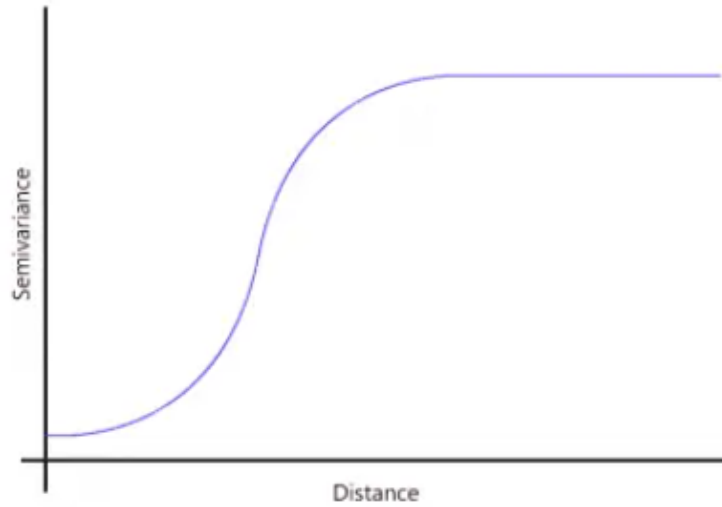


Figure 2.10: Gaussian variogram model

• **Cubic Model**

This model is valid in three dimensions.

$$\gamma(h) = \begin{cases} c_0 + c \left(-7 \left(\frac{h}{a} \right)^2 - \frac{35}{4} \left(\frac{h}{a} \right)^3 + \frac{7}{2} \left(\frac{h}{a} \right)^5 - \frac{3}{4} \left(\frac{h}{a} \right)^7 \right), & \text{for } 0 < h \leq a \\ c_0 + c, & \text{for } h > a \\ c_0, & \text{for } h = 0 \end{cases} \quad (2.14)$$

The parameters a , c_0 and $c_0 + c$ are the range, the nugget, and the sill respectively.

• **Matérn Model**

The Matérn model is a generalization of several models as exponential and Gaussian models. It is valid for any dimension and its formula defined as the following

$$\gamma(h) = c_0 + c \left(1 - \frac{1}{2^{\nu-1}\Gamma(\nu)} \left(\frac{h}{a} \right)^{\nu} \mathcal{K}_{\nu} \left(\frac{h}{a} \right) \right), \quad (2.15)$$

where $\mathcal{K}_\nu(x)$ is the modified Bessel function of second kind of order ν , a is the distance parameter, c_0 is the nugget, and c is the sill. The case $\nu = \frac{1}{2}$ gives the exponential model and $\nu = \infty$ gives the Gaussian model.

• **Pure Nugget Model** In practice, due to measurement error the empirical variogram does not approach to 0 as the lag distance converges to 0. We define a pure nugget variogram as

$$\gamma(h) = c_0(1 - \delta(h)), \quad (2.16)$$

where c_0 is the variance and

$$\delta(h) = \begin{cases} 1, & \text{if } h = 0 \\ 0, & \text{otherwise.} \end{cases} \quad (2.17)$$



Figure 2.11: Pure nugget model

• **Combining Models (Nested Models)** All previous models have simple formula with simple shapes. However, in many cases the variogram shape appears more

complex and therefore we need more complex models to describe it. The best way to do this is to combine two or more simple models, for example of combining models is the nested spherical, or double spherical model with nugget equal to zero. Its formula is giving by

$$\gamma(h) = \begin{cases} c_1 \left\{ 1.5 \frac{h}{a_1} - 0.5 \left(\frac{h}{a_1} \right)^3 \right\} + c_2 \left\{ 1.5 \frac{h}{a_2} - 0.5 \left(\frac{h}{a_2} \right)^3 \right\} & \text{for } 0 < h \leq a_1, \\ c_1 + c_2 \left\{ 1.5 \frac{h}{a_2} - 0.5 \left(\frac{h}{a_2} \right)^3 \right\} & \text{for } a_1 < h \leq a_2, \\ c_1 + c_2 & \text{for } h > a_2 \end{cases} \quad (2.18)$$

2.4 Fitting variogram model

In Section 2.3 we listed some of commonly used semivariograms. In this section, we will estimate the model parameters to fit one of these variogram models. Consider the empirical semivariogram values $\hat{\gamma}(h)$ are our observations and $\gamma(h, \beta)$ are the predicted values based on some model, where $\beta = (c, c_0, a)'$ is a vector of parameters. Zimmerman and Zimmerman [41] proposed seven methods to estimate the semivariogram parameters. *Ordinary least squares (OLS)*, *Cressie's weighted least squares (WLS-1 and WLS-2)*, *Delfiner's weighted least squares (WLS-3)*, *maximum likelihood (ML)*, *restricted maximum likelihood (REML)* and *generalized minimum variance quadratic un-biased (GMIVQU) estimator*. They compared the performance of these methods by the Monte Carlo simulation and showed that ordinary least squares (OLS) provides the best performance in many cases.

2.5 Kriging

Danie Krige was a South African statistician and mining engineer. He estimated the distribution of gold grades at Witwatersrand complex in South Africa based on samples from few locations. This technique is named kriging [12].

Let $\{Z(s_i)\}$ be the values at locations s_i , $i = 1, 2, \dots, n$. The aim of kriging is to estimate the value of $Z(s_0)$ at unsampled location s_0 . The most common type of kriging is the **ordinary kriging** which is based on weighted averages of the sampled values $Z(s_1), Z(s_2), \dots, Z(s_n)$. The ordinary kriging estimator is defined by

$$\hat{Z}_0 = \hat{Z}(s_0) = \sum_{i=1}^n w_i Z(s_i) = \sum_{i=1}^n w_i Z_i = [w_1 \quad w_2 \quad \dots \quad w_n] \begin{bmatrix} Z_1 \\ Z_2 \\ \vdots \\ Z_n \end{bmatrix} =$$

$$\mathbf{w}'_1 \mathbf{Z}, \tag{2.19}$$

where Z_i is the i^{th} sample value and w_i is the weight for Z_i , $i = 1, 2, \dots, n$. To insure the estimator in Eq. (2.19) is unbiased we have two assumptions [35]

- $\sum_{i=1}^n w_i = 1$,
- $E(\hat{Z}(s_0) - Z(s_0)) = 0$.

The estimator $\hat{Z}_0 = \mathbf{w}'\mathbf{Z}$ is said to be a **best linear unbiased predictor (BLUP)**

if the following conditions satisfied:

- Unbiased, that is $E(\hat{Z}_0) = E(Z_0)$. This will be satisfied if $\sum_{i=1}^n w_i = 1$ and $E(Z_i) = \mu$ for $i = 1, 2, \dots, n$.
- The mean square prediction error (MSPE) $\sigma_\epsilon^2 = E(Z_0 - \hat{Z}_0)^2 = \text{Var}((Z_0 - \hat{Z}_0))$ is minimized.

The weights are based on the covariance among the sampled values, $\text{Cov}(Z(s_i), Z(s_j))$, and the covariance between sample values and the predicted value $\hat{Z}(s_0)$, where

$$\mathbf{C}_1 = \begin{pmatrix} C_{11} & C_{1,2} & \cdots & C_{1n} \\ C_{2,1} & C_{22} & \cdots & C_{2n} \\ \vdots & \vdots & \cdots & \vdots \\ C_{n1} & C_{n2} & \cdots & C_{nn} \end{pmatrix}, \quad (2.20)$$

such that $C_{ij} = C(s_i, s_j) = \text{Cov}(Z(s_i), Z(s_j))$, $\forall i, j = 1, 2, \dots, n$ and the covariance vector between the sample values and the predicted value is defined by

$$\mathbf{c}_0 = \begin{pmatrix} C_{10} \\ C_{20} \\ \vdots \\ C_{n0} \end{pmatrix}, \quad (2.21)$$

where $C_{i0} = C(s_i, s_0) = \text{Cov}(Z(s_i), \hat{Z}(s_0))$, $\forall i = 1, 2, \dots, n$.

The mean square prediction error (MSPE) can be written as

$$\begin{aligned} \sigma_\epsilon^2 &= \text{Var}(Z_0 - \hat{Z}_0) = \text{Var}(Z_0) + \text{Var}(\hat{Z}_0) - 2\text{Cov}(\hat{Z}_0, Z_0) \\ &= \sigma^2 + \text{Var}(\sum_{i=1}^n w_i Z_i) - 2\text{Cov}(\sum_{i=1}^n w_i Z_i, Z_0) \\ &= \sigma^2 + \sum_{i=1}^n \sum_{j=1}^n w_i w_j \text{Cov}(Z_i Z_j) - 2 \sum_{i=1}^n w_i \text{Cov}(Z_i, Z_0) \end{aligned}$$

which implies that

$$\sigma_\epsilon^2 = \text{Var}(Z_0 - \hat{Z}_0) = \sigma^2 + \sum_{i=1}^n \sum_{j=1}^n w_i w_j C_{ij} - 2 \sum_{i=1}^n w_i C_{i0}, \quad (2.22)$$

In order to minimize $\text{Var}(Z_0 - \hat{Z}_0)$ subject to $\sum_{i=1}^n w_i = 1$ we use the **Lagrange multiplier** method [3]. The Lagrangian function is defined as

$$\mathcal{L}(\mathbf{w}, \lambda) = \text{Var}(Z_0 - \hat{Z}_0) + 2\lambda(\sum_{i=1}^n w_i - 1), \quad (2.23)$$

Therefore,

$$\mathcal{L}(\mathbf{w}, \lambda) = \sigma^2 + \sum_{i=1}^n \sum_{j=1}^n w_i w_j C_{ij} - 2 \sum_{i=1}^n w_i C_{i0} + 2\lambda(\sum_{i=1}^n w_i - 1) \quad (2.24)$$

Now we want to solve $\nabla_{\mathbf{w}, \lambda} \mathcal{L}(\mathbf{w}, \lambda) = 0$, where ∇ is called the gradient which is the partial derivatives of λ at (\mathbf{w}, λ) . This implies that

$$\begin{cases} 2 \sum_{j=1}^n w_j C_{1j} - 2C_{10} + 2\lambda = 0 \\ 2 \sum_{j=1}^n w_j C_{2j} - 2C_{20} + 2\lambda = 0 \\ \vdots \\ 2 \sum_{j=1}^n w_j C_{nj} - 2C_{n0} + 2\lambda = 0 \\ 2(\sum_{j=1}^n w_j - 1) = 0. \end{cases} \quad (2.25)$$

We rewrite the system of linear equations in (2.25) as

$$\begin{cases} \sum_{j=1}^n w_j C_{1j} + \lambda = C_{10} \\ \sum_{j=1}^n w_j C_{2j} + \lambda = C_{20} \\ \vdots \\ \sum_{j=1}^n w_j C_{nj} + \lambda = C_{n0} \\ \sum_{j=1}^n w_j \cdot 1 + 0 = 1. \end{cases} \quad (2.26)$$

The system of linear equations in 2.26 can be written in a matrix form

$$\begin{pmatrix} C_{11} & \cdots & C_{1n} & 1 \\ C_{21} & \cdots & C_{2n} & 1 \\ \vdots & & \vdots & \vdots \\ C_{n1} & \cdots & C_{nn} & 1 \\ 1 & \cdots & 1 & 0 \end{pmatrix} \begin{pmatrix} w_1 \\ w_2 \\ \vdots \\ w_n \\ \lambda \end{pmatrix} = \begin{pmatrix} C_{10} \\ C_{20} \\ \vdots \\ C_{n0} \\ 1 \end{pmatrix}. \quad (2.27)$$

Using the matrix in (2.20) and the vector in (2.21), the matrix equation in 2.27 can be written as a partition matrix

$$\left(\begin{array}{c|c} \mathbf{C}_1 & \mathbf{1} \\ \hline \mathbf{1}' & 0 \end{array} \right) \begin{pmatrix} \mathbf{w}_1 \\ \lambda \end{pmatrix} = \begin{pmatrix} \mathbf{c}_0 \\ 1 \end{pmatrix}, \quad (2.28)$$

where $\mathbf{w}_1 = (w_1 \ w_2 \ \cdots \ w_n)'$.

Let $\mathbf{C} = \left(\begin{array}{c|c} \mathbf{C}_1 & \mathbf{1} \\ \hline \mathbf{1}' & 0 \end{array} \right)$, $\mathbf{w} = \begin{pmatrix} \mathbf{w}_1 \\ \lambda \end{pmatrix}$ and $\mathbf{D} = \begin{pmatrix} \mathbf{c}_0 \\ 1 \end{pmatrix}$, then the weights for the

ordinary kriging can be obtained by solving

$$\mathbf{w} = \begin{pmatrix} \mathbf{w}_1 \\ \lambda \end{pmatrix} = \left(\begin{array}{c|c} \mathbf{C}_1 & \mathbf{1} \\ \hline \mathbf{1}' & 0 \end{array} \right)^{-1} \begin{pmatrix} \mathbf{c}_0 \\ 1 \end{pmatrix} = \mathbf{C}^{-1} \mathbf{D}. \quad (2.29)$$

Applying the inverse of the partitioned matrix on the matrix $\left(\begin{array}{c|c} \mathbf{C}_1 & \mathbf{1} \\ \hline \mathbf{1}' & 0 \end{array} \right)$, the weights can

be written as

$$\mathbf{w}_1 = \mathbf{C}_1^{-1} \mathbf{c}_0 - \frac{\mathbf{c}_1^{-1} \mathbf{1} \mathbf{c}_1^{-1} \mathbf{c}_0}{\mathbf{1}' \mathbf{c}_1^{-1} \mathbf{1}} + \frac{\mathbf{c}_1^{-1} \mathbf{1}}{\mathbf{1}' \mathbf{c}_1^{-1} \mathbf{1}}, \quad (2.30)$$

where (2.28) is known as kriging equation.

To write the mean square prediction error (MSPE) $\sigma_\epsilon^2 = \text{Var}(Z_0 - \hat{Z}_0)$ in terms of kriging estimates, we multiply the i th equation in 2.27 by w_i and sum the first n equations, we get

$$\sum_{i=1}^n w_i \sum_{j=1}^n w_j C_{ij} + \sum_{i=1}^n w_i \lambda = \sum_{i=1}^n w_i C_{i0}. \quad (2.31)$$

Therefore,

$$\sum_{i=1}^n \sum_{j=1}^n w_i w_j C_{ij} = \sum_{i=1}^n w_i C_{i0} - \lambda. \quad (2.32)$$

Substituting Eq. (2.32) in Eq. (2.22), we have

$$\sigma_\epsilon^2 = \sigma^2 - (\sum_{i=1}^n w_i C_{i0} + \lambda). \quad (2.33)$$

Writing Eq. (2.33) in matrix form, we get

$$\sigma_\epsilon^2 = \sigma^2 - (w_1 \quad w_2 \quad \cdots \quad w_n \mid \lambda) \begin{pmatrix} C_{10} \\ C_{20} \\ \vdots \\ C_{n0} \\ 1 \end{pmatrix} = \sigma^2 - (\mathbf{w}_1 \mid \lambda) \begin{pmatrix} \mathbf{c}_0 \\ 1 \end{pmatrix}. \quad (2.34)$$

Therefore,

$$\sigma_\epsilon^2 = \sigma^2 - \mathbf{w}'\mathbf{D}. \quad (2.35)$$

Now we would like to write the kriging equations in (2.28) in terms of the semivariogram instead of the covariances. We showed in Eq. (2.4) that the semivariogram can be written in terms of covariance function as $\gamma_{ij} = \frac{1}{2}\text{Var}(Z_i - Z_j) = \sigma^2 - C_{ij}$, which implies that $C_{ij} = \sigma^2 - \gamma_{ij}$.

Therefore, the matrices (2.20) and (2.21) can be written as

$$\mathbf{C}_1 = \begin{pmatrix} C_{11} & \cdots & C_{1n} \\ \vdots & \ddots & \vdots \\ C_{n1} & \cdots & C_{nn} \end{pmatrix} = \begin{pmatrix} \sigma^2 & \cdots & \sigma^2 \\ \vdots & \ddots & \vdots \\ \sigma^2 & \cdots & \sigma^2 \end{pmatrix} - \begin{pmatrix} \gamma_{11} & \cdots & \gamma_{1n} \\ \vdots & \ddots & \vdots \\ \gamma_{n1} & \cdots & \gamma_{nn} \end{pmatrix} = \sigma^2 \mathbf{1}\mathbf{1}' - \mathbf{\Gamma}_1 \quad (2.36)$$

and

$$\mathbf{c} = \begin{pmatrix} C_{10} \\ \vdots \\ C_{n0} \end{pmatrix} = \begin{pmatrix} \sigma^2 \\ \vdots \\ \sigma^2 \end{pmatrix} - \begin{pmatrix} \gamma_{10} \\ \vdots \\ \gamma_{n0} \end{pmatrix} = \sigma^2 \mathbf{1} - \mathbf{\Gamma}_0. \quad (2.37)$$

Substituting (2.36) and (2.37) in the matrix partition (2.28), the kriging equations can be written in terms of the semivariogram as follows

$$\left(\begin{array}{c|c} \mathbf{C}_1 & \mathbf{1} \\ \hline \mathbf{1}' & 0 \end{array} \right) \begin{pmatrix} \mathbf{w}_1 \\ \lambda \end{pmatrix} = \begin{pmatrix} \mathbf{c}_0 \\ 1 \end{pmatrix} \Leftrightarrow \left(\begin{array}{c|c} \sigma^2 \mathbf{1}\mathbf{1}' - \Gamma_1 & \mathbf{1} \\ \hline \mathbf{1}' & 0 \end{array} \right) \begin{pmatrix} \mathbf{w}_1 \\ \lambda \end{pmatrix} = \begin{pmatrix} \sigma^2 \mathbf{1} - \Gamma_0 \\ 1 \end{pmatrix}, \quad (2.38)$$

which implies that

$$\begin{pmatrix} \sigma^2 \mathbf{1}\mathbf{1}' \mathbf{w}_1 - \Gamma_1 \mathbf{w}_1 + \lambda \mathbf{1} \\ \mathbf{1}' \mathbf{w}_1 \end{pmatrix} = \begin{pmatrix} \sigma^2 \mathbf{1} - \Gamma_0 \\ 1 \end{pmatrix}, \quad (2.39)$$

since $\mathbf{1}' \mathbf{w}_1 = \sum_{i=1}^n w_i = 1$ then $\sigma^2 \mathbf{1}\mathbf{1}' \mathbf{w}_1 = \sigma^2 \mathbf{1}$.

Therefore,

$$\begin{pmatrix} -\Gamma_1 \mathbf{w}_1 + \lambda \mathbf{1} \\ \mathbf{1}' \mathbf{w}_1 \end{pmatrix} = \begin{pmatrix} -\Gamma_0 \\ 1 \end{pmatrix} \Leftrightarrow \left(\begin{array}{c|c} -\Gamma_1 & \mathbf{1} \\ \hline \mathbf{1}' & 0 \end{array} \right) \begin{pmatrix} \mathbf{w}_1 \\ \lambda \end{pmatrix} = \begin{pmatrix} -\Gamma_0 \\ 1 \end{pmatrix}, \quad (2.40)$$

hence the weights can be written as

$$\mathbf{w}_1 = \Gamma_1^{-1} \Gamma_0 - \frac{\Gamma_1^{-1} \mathbf{1}\mathbf{1}' \Gamma_1^{-1} \Gamma_0}{\mathbf{1}' \Gamma_1^{-1} \mathbf{1}} + \frac{\Gamma_1^{-1} \mathbf{1}}{\mathbf{1}' \Gamma_1^{-1} \mathbf{1}}. \quad (2.41)$$

CHAPTER 3: VARIOGRAM MODELLING FOR STURCTURAL MRI DATA

3.1 Data Description

3.1.1 Image format

In this section, we will use the variogram approach to model the spatial coorelation in neuroimaging data. We use data that is available from the Coursera Course **Introduction to Neurohacking In R** [1]. The file types that we are working on them are *DICOM* (Digital Inaging and Communications in Medicine) format (.dcm) and *NIFTI* (Neuroimaging Informatics Technology Initiative) formate (.nii, .nii.gz). The main difference between these two files is that the DICOM file represents one slice of the brain where the NIFTI file represents three dimensional image of the brain. We have 22 DICOM files which mean 22 slices of the brain, each image is a matrix with dimension of each 288×288 pixels, the dimension of each pixel is 0.7986×0.7986 mm (see Fig. 3.1). The first step is to read the numbers corresponding to each pixel of each brain slice. These numbers represent the color intensity of the image which will be the data of this work. To read these data we use **R** and the function **readDICOM** from **oro.dicom** package ([33], [38]).

Fig. 3.2 shows the dicom images of slices 10, 11, and 12. We select these images because the lighter spot in these images represent a brain tumor which will be the region of interest.

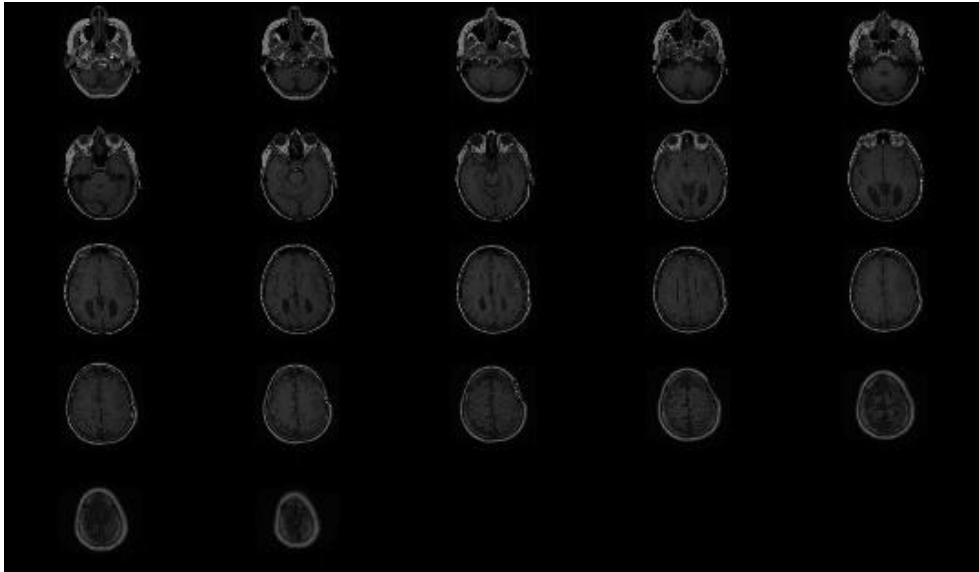
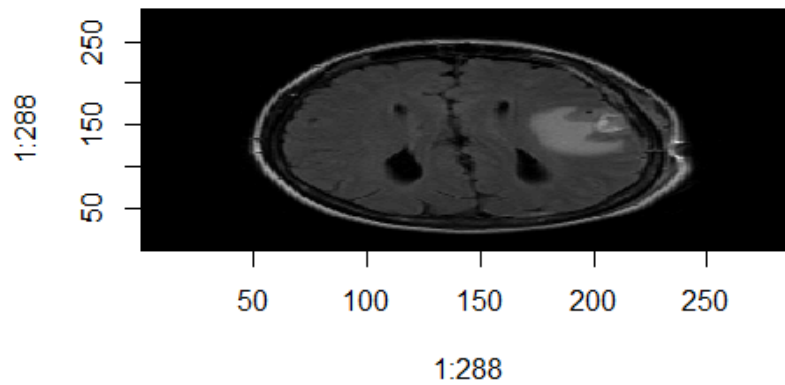
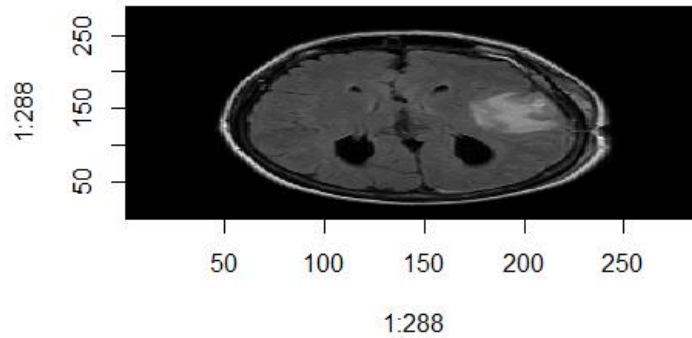


Figure 3.1: 22 axial slice image of the brain, the slices starts from the bottom to top of the head

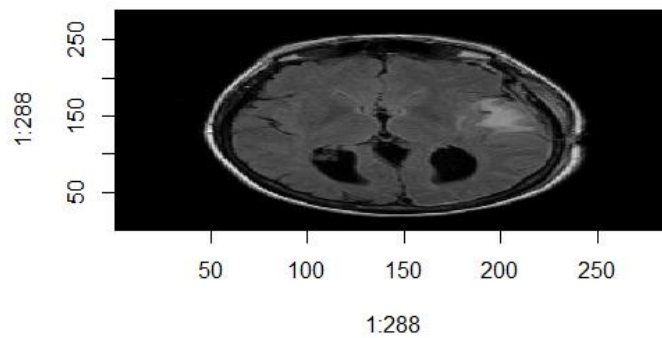


(a) Slice 10

Figure 3.2 DICOM images of the 10th, 11th , and 12th slice of the brain with dimension 288 × 288 pixel.



(b) Slice 11



(c) Slice 12

Figure 3.2: DICOM images of the 10th, 11th and 12th slice of the brain with dimension 288×288 pixel.

3.1.2 Masking the brain

In this process, we mask the brain because we want to remove the non-interest regions of brain structure before performing any statistical analysis. This step can be done by using the ROI image (**R**egion **O**f **I**nterest image). ROI image correspond to a binary matrix with two values 1 for the white color which represents the tumor region and 0 for the black color (see Fig. 3.3) ([10], [27]).

To read the data image of the tumor region we multiply each matrix of images in Fig. 3.2 with the corresponding elements of the ROI matrices in Fig. 3.3a, 3.3c, and 3.3e. Then, we get a matrix with values of the interest region voxels and 0 values for

the non-interest region (see Table 3.2). Therefore, the number of voxels in the tumor region of each slice in Fig. 3.2 are

Table 3.1: Number of voxels for the tumor region in the slices 10, 11 and 12

Slice Number	Number of Voxels
Slice 10	1902
Slice 11	1807
Slice 12	1044

Fig. 3.3b, 3.3d, and 3.3f are plots of ROI images as spatial data, each color represents an interval of values at specific locations. The plots show that the values of these voxels increased as we move from outside to inside tumor region.

Table 3.2: A matrix of numbers correspond to 195 to 210 voxel in the x direction and 130 to 140 voxel in the y direction of the brain slice in figure 16

	[,1]	[,2]	[,3]	[,4]	[,5]	[,6]	[,7]	[,8]	[,9]	[,10]	[,11]
[1,]	217	218	227	248	255	248	229	190	160	178	209
[2,]	217	219	239	258	254	237	221	201	172	149	152
[3,]	229	240	251	240	222	221	230	217	174	135	145
[4,]	254	263	249	233	233	227	219	230	213	143	107
[5,]	236	251	258	263	272	254	223	225	226	170	112
[6,]	254	250	247	260	269	259	245	241	229	189	149
[7,]	244	237	229	244	264	264	254	259	251	198	148
[8,]	215	220	229	240	257	264	258	260	251	212	187
[9,]	248	246	245	251	258	256	253	256	241	204	198
[10,]	252	260	261	265	269	261	253	252	229	173	155
[11,]	244	253	259	253	239	233	250	257	209	136	142
[12,]	256	246	244	253	250	246	260	249	163	62	88
[13,]	256	261	240	218	225	239	223	160	66	2	50
[14,]	256	269	220	132	83	94	97	56	17	29	87
[15,]	249	226	179	116	58	30	23	24	44	70	75
[16,]	241	221	203	177	124	54	13	2	36	82	96

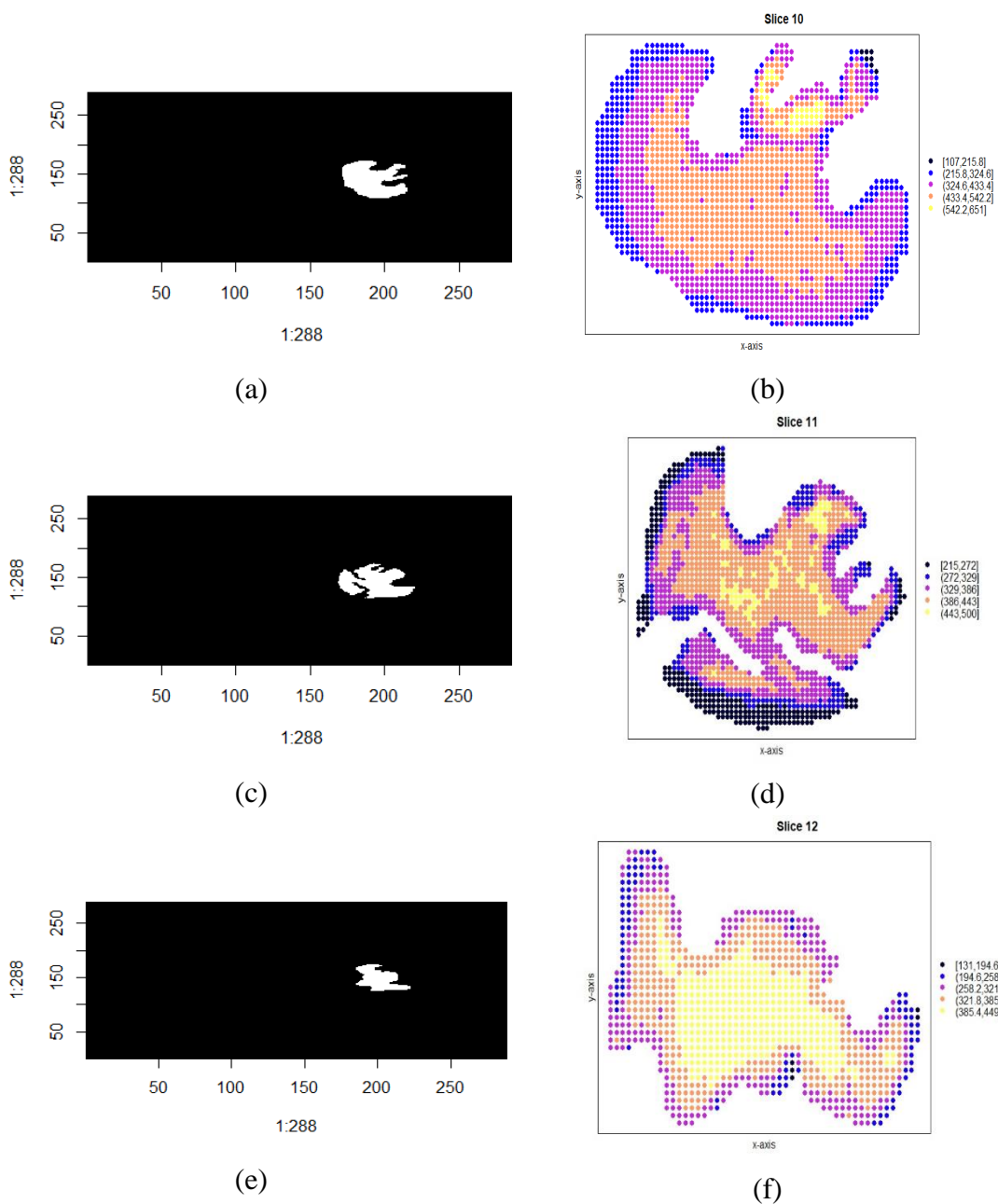


Figure 3.3: Panels (a), (c) and (e) represent the ROI images of the 10th, 11th, and 12th slice of the brain respectively and panels (b), (d), (f) are plots ROI images as spatial data

3.2 Variogram modelling

Data are collected from specific voxels related to tumor regions in slices 10, 11, and 12. In each slice, we calculate the empirical variogram and we use the K -fold cross validation to choose between different variogram models based on their kriging results [27]. Consider the voxels values $Z(s_1), Z(s_2), \dots, Z(s_N)$ at locations s_1, s_2, \dots, s_N . The K -fold cross validation splits the N voxels into K folds, each fold has n voxels $Z(s_1^l), Z(s_2^l), \dots, Z(s_n^l)$, where $n = \frac{N}{K}$ and $l = 1, 2, \dots, K$. The voxel values $Z(s_1^l), Z(s_2^l), \dots, Z(s_n^l)$ in each fold removed and the voxel values in the other folds are used to predict new values at the locations $s_1^l, s_2^l, \dots, s_n^l$ by using kriging. Letting $\hat{Z}(s_1^l), \hat{Z}(s_2^l), \dots, \hat{Z}(s_n^l)$ be the kriging values predicted at locations $s_1^l, s_2^l, \dots, s_n^l$ with kriging variances $\sigma^2(s_1^l), \sigma^2(s_2^l), \dots, \sigma^2(s_n^l)$, the mean squared deviation ratio (MSDR) is defined as the mean square error (MSE) divided by the kriging variances and it is calculated as follows [39]

$$MSDR = \frac{1}{N} \sum_{l=1}^K \sum_{i=1}^n \frac{(Z(s_i^l) - \hat{Z}(s_i^l))^2}{\sigma^2(s_i^l)}. \quad (3.1)$$

- When $MSDR > 1$, the kriging variance underestimates the true estimation variance.
- When $MSDR < 1$, the kriging variance exaggerates the true estimation variance.
- When $MSDR \approx 1$, the accurate estimated error equals the error predicted by the model.

For the selected variogram model, we want the MSDR to approach the value 1.

We compute the variance for any two locations s_i and s_j as

$$\gamma(s_i, s_j) = \frac{1}{2} (Z(s_i) - Z(s_j))^2. \quad (3.2)$$

The values are plotted against the distance (lag) as a scatter diagram, called the

variogram cloud. We calculate the empirical variogram using Eq. (2.5). Fig. 3.4a, 3.4c, and 3.4e show the variogram cloud for the tumor region in the aforementioned slices while Fig. 3.4b, 3.4d, and 3.4f show the empirical variogram graphs for these slices.

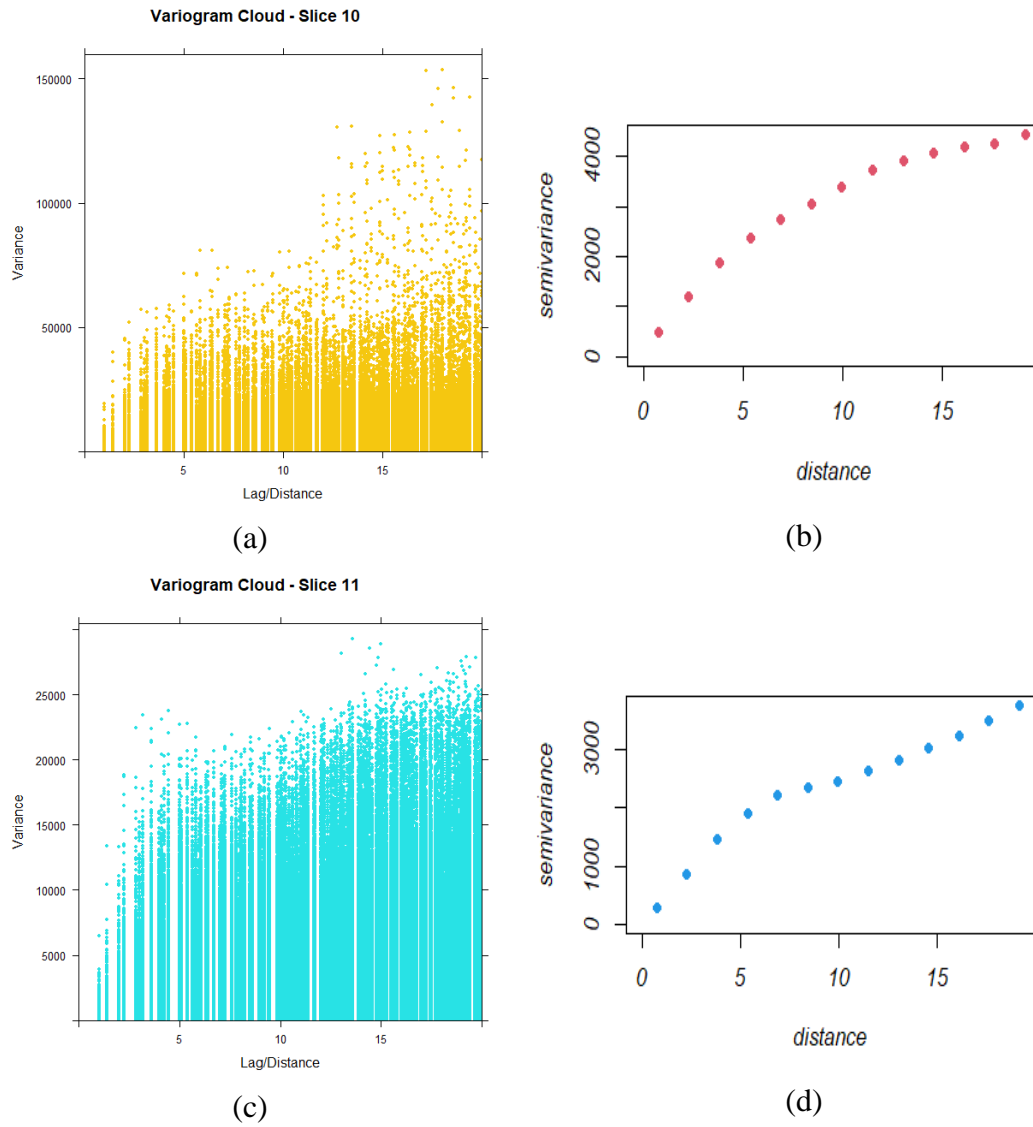


Figure 3.4: Panels (a) and (c) show the variogram cloud for the image data in slices 10 and 11 respectively while panels (b) and (d) show the empirical variogram of these data.

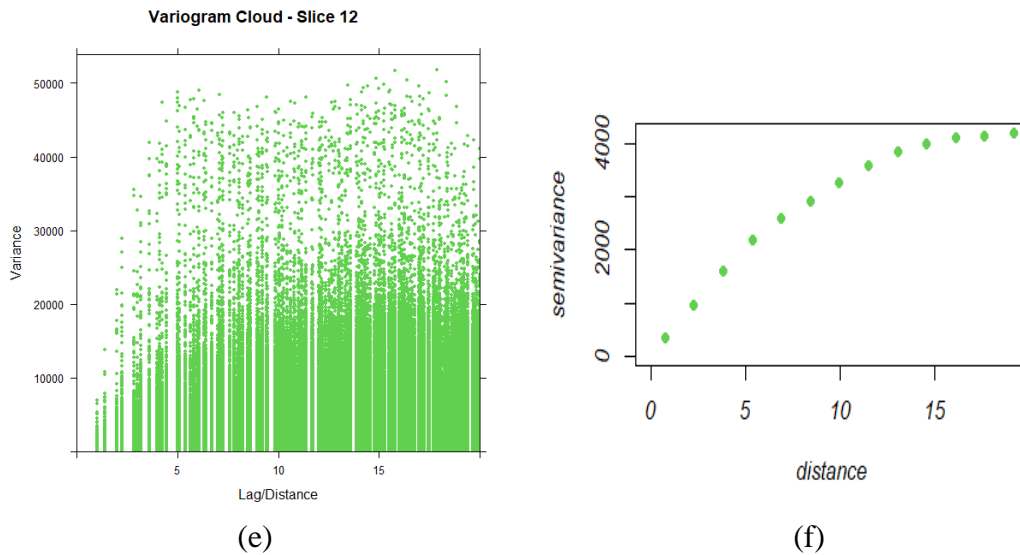


Figure 3.4: Panel (e) shows the variogram cloud for the image data in slice 12 while panel (f) shows the empirical variogram of this data.

3.2.1 Validation of Stationary assumption

The first step prior to variogram modeling is to check the validation of the second order stationary of the data. This can be done by computing the global variogram as in Fig. 3.4 and local variogram. The local empirical variograms are calculated by using the moving windows method. We calculate and plot the local variograms for randomly selected points of the interest region (see Fig. 3.5, 3.6, and 3.7). It can be seen that the shapes and the variogram parameters are very close to those of the global variograms ([8], [16], [17], [39]). Local variogram at other randomly points gives similar results. This implies that the second order stationary assumption is valid for the image data in slices 10, 11 and 12.

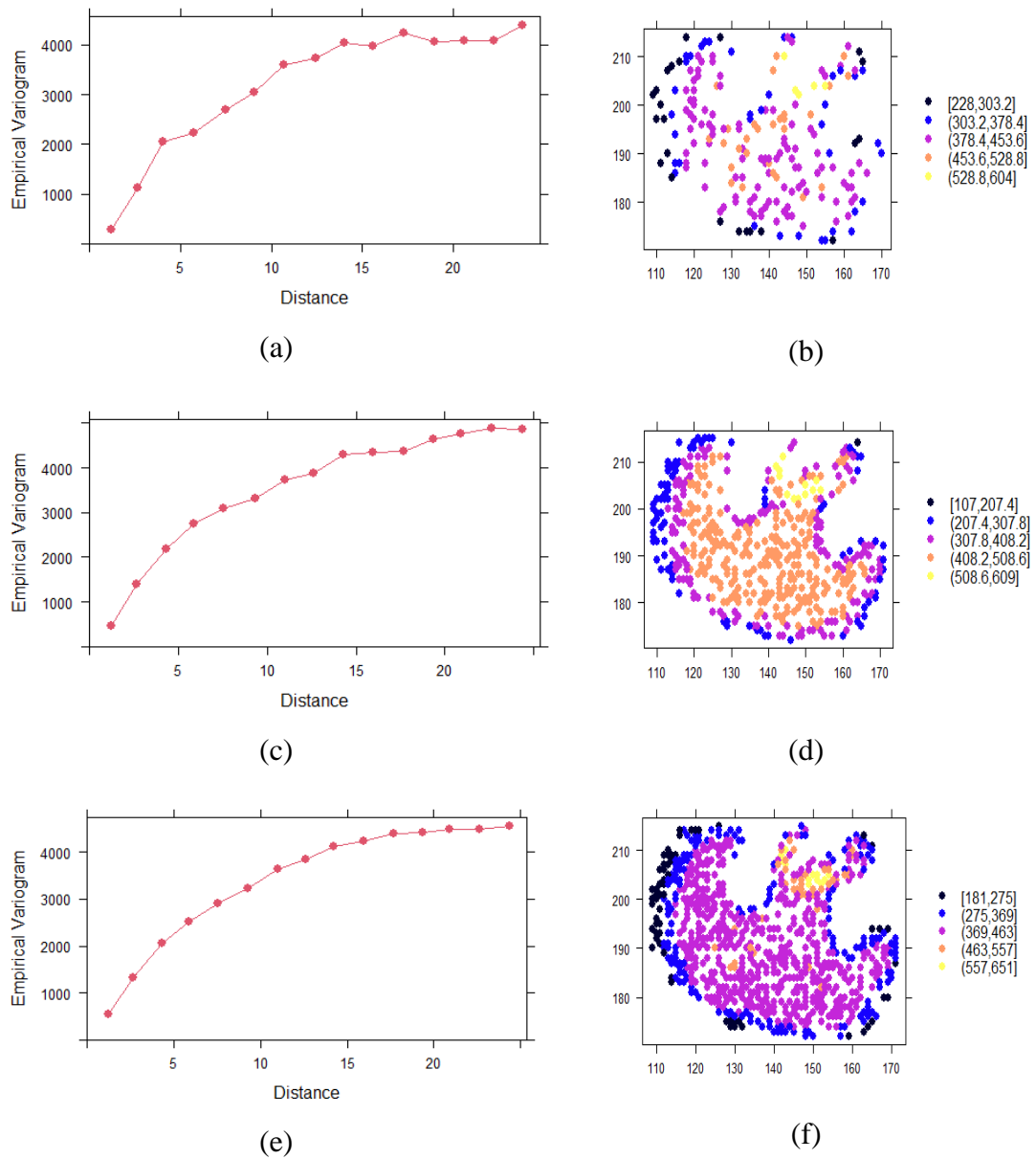
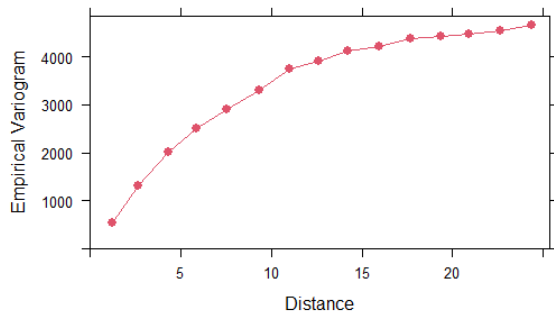
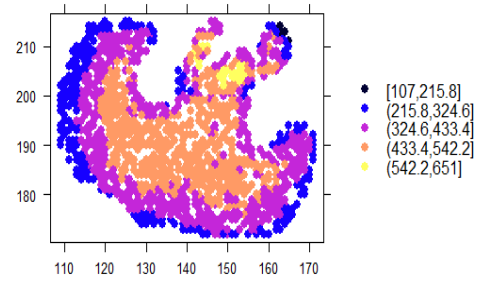


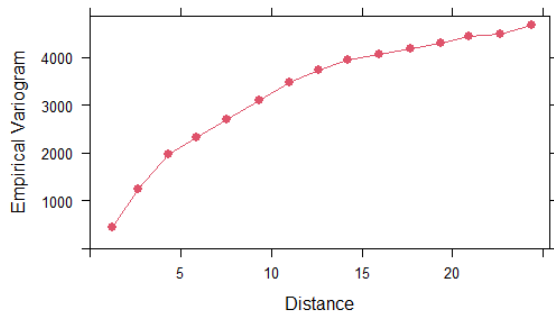
Figure 3.5: Panels (a), (c), and (e) are local variograms for the corresponding randomly selected points of slice 10 in panels (b), (d), and (f). The numbers of selected points in panels (b), (d), and (f) are 200, 500, and 800 respectively.



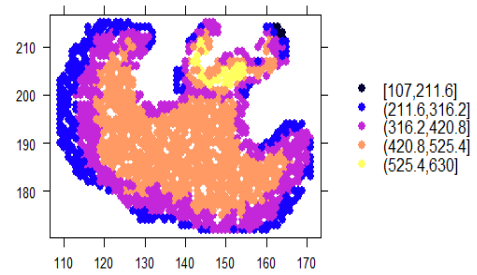
(g)



(h)

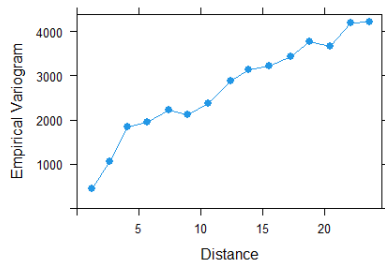


(i)

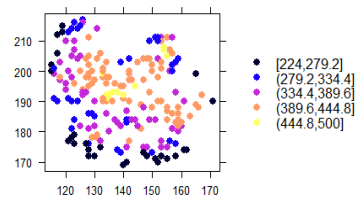


(j)

Figure 3.5: Panel (g) and (i) are the local variograms for the corresponding randomly selected points of slice 10 in panels (h) and (j). The numbers of selected points in panels (h) and (j) are 1200 and 1500 respectively.

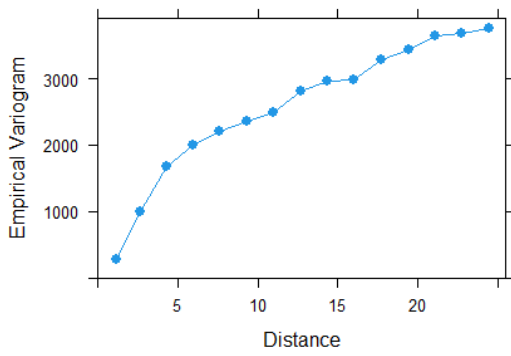


(a)

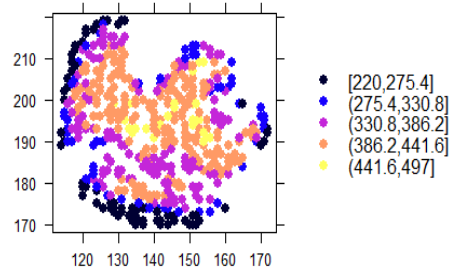


(b)

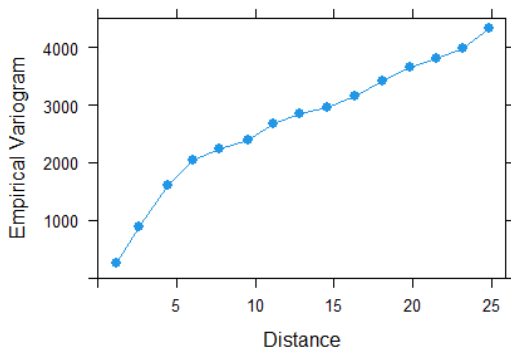
Figure 3.6: Panels (a) is local variogram for the corresponding randomly selected points of slice 11 in panel (b). The number of selected points in panel (b) is 200.



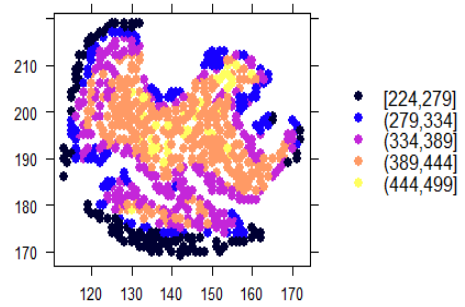
(c)



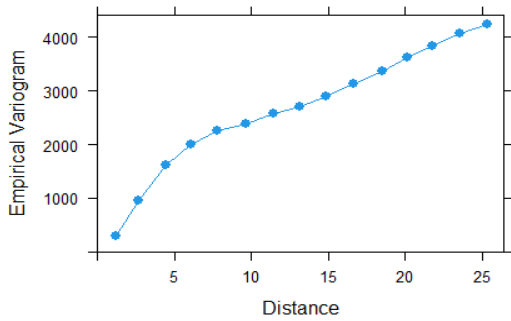
(d)



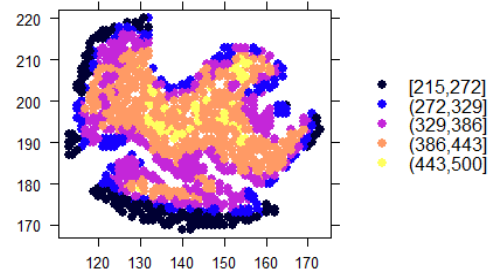
(e)



(f)



(g)



(h)

Figure 3.6: Panels (c), (e), and (g) are local variograms for the corresponding randomly selected points of slice 11 in panels (d), (f), and (h). The number of selected points in panels (d), (f), and (h) are 500, 800, and 1200 respectively.

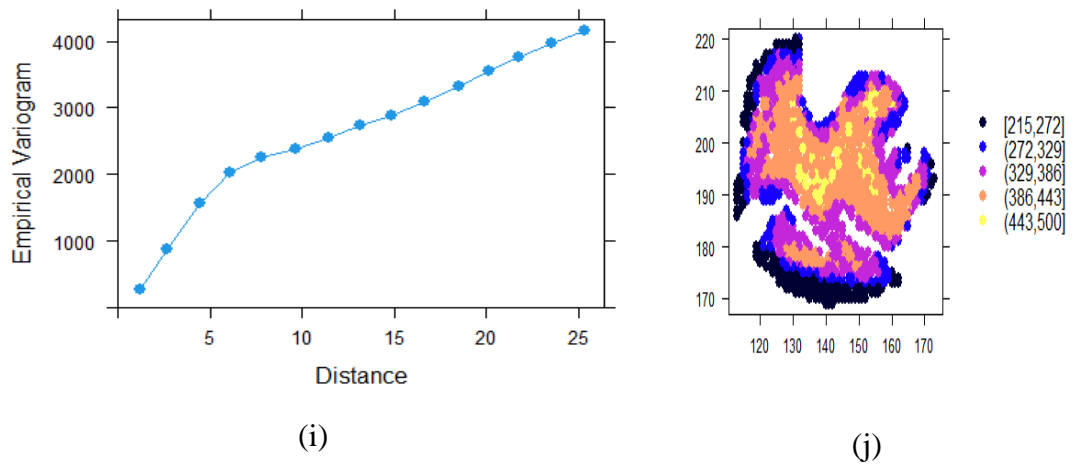


Figure 3.6: Panels (i) is local variogram for the corresponding randomly selected points of slice 11 in panel (j). The number of selected points in panel (j) is 1500.

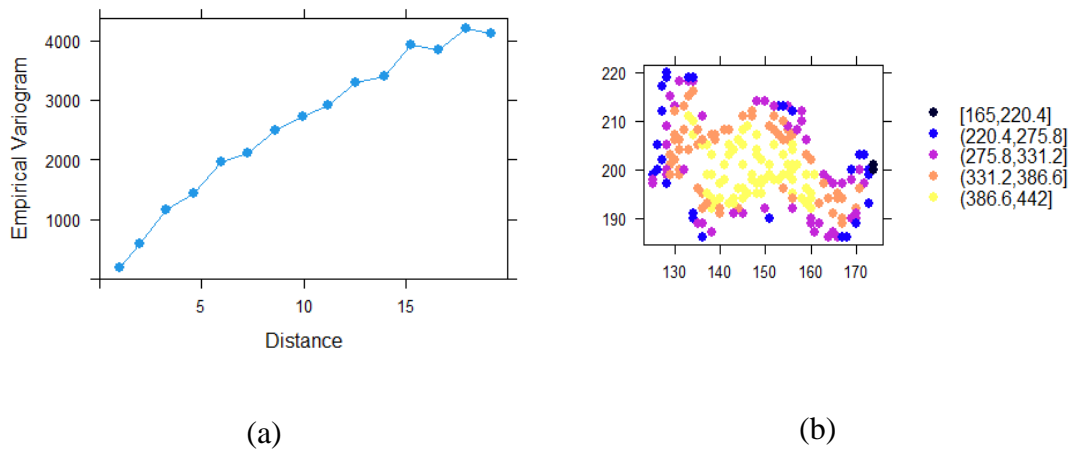
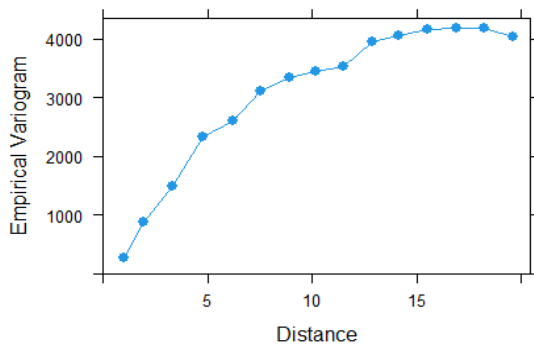
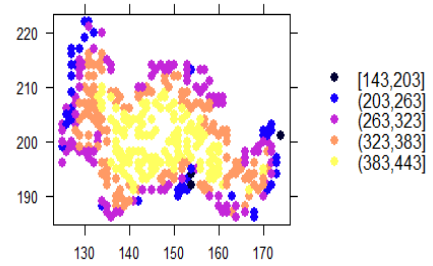


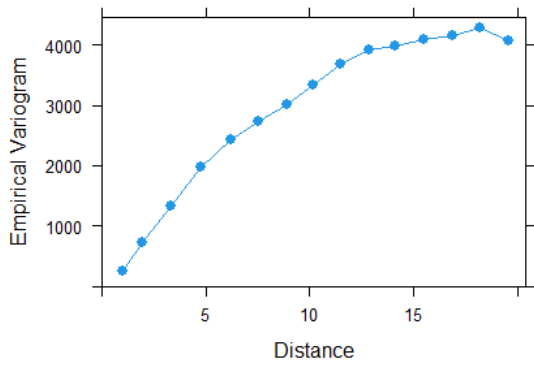
Figure 3.7: Panel (a) is the local variogram for the corresponding randomly selected points of slice 12 in panel (b). The number of selected points in panel (b) is 200.



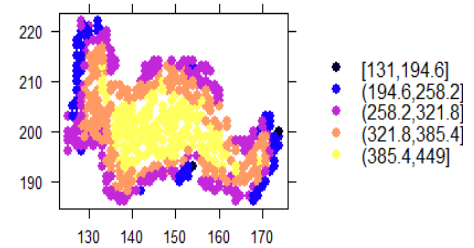
(c)



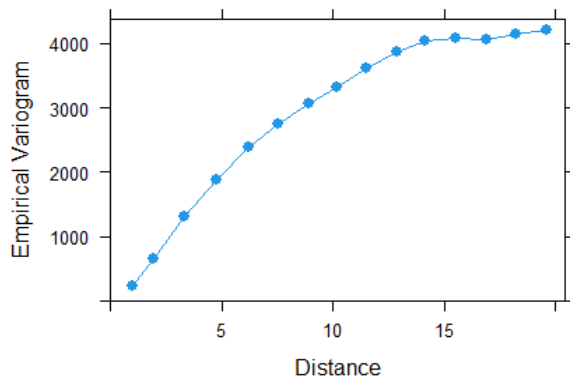
(d)



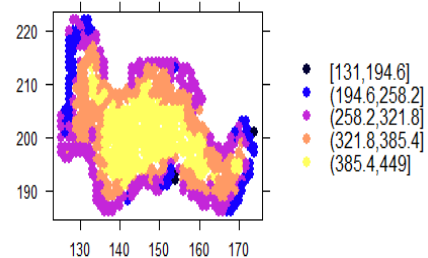
(e)



(f)



(g)



(h)

Figure 3.7: Panels (c), (e), and (g) are local variograms for the corresponding randomly selected points of slice 12 in panels (d), (f), and (h). The number of selected points in panels (d), (f), and (h) are 400, 600, and 800 respectively.

3.2.2 Validation of Isotropy Assumption

Rose diagram is a graphic tool used to give a brief view of how we can identify a spatial correlation structure in different directions ([2], [20]). The diagram places spikes releasing from the origin of a circle in different directions, the length of each spike corresponding to a selected variogram value for each direction. Fig. 3.8 – 3.10 display the rose diagrams of the empirical variogram in different directions for the data in slices 10, 11 and 12 respectively. It is clear that an anisotropy exist.

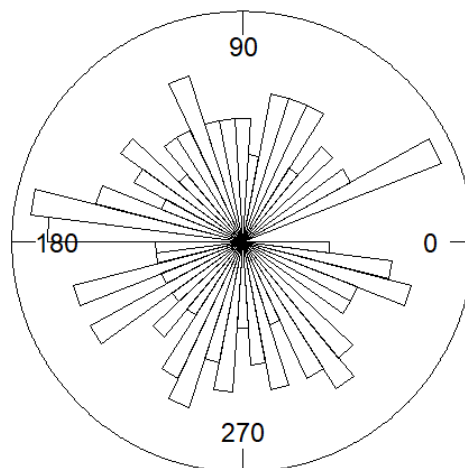


Figure 3.8: Rose diagram of the empirical variogram for data in slice 10

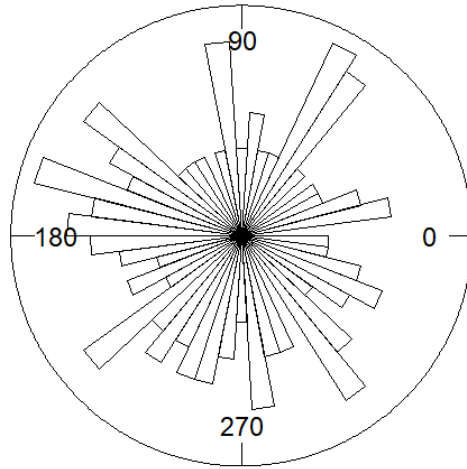


Figure 3.9: Rose diagram of the empirical variogram for data in slice 11

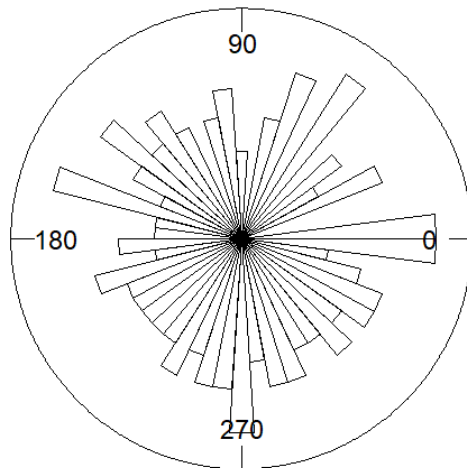


Figure 3.10: Rose diagram of the empirical variogram for data in slice 12

Using a lag spacing of 1, horizontal and vertical tolerance of 5 degrees, maximum distance between points of 20 and angles of 60°, 90°, and 120° we compute the empirical variogram of the data in slices 10, 11, and 12 ([26], [31]). Fig. 3.11 shows the directional variogram of the aforementioned slices at angles 60°, 90°, and 120°. The nugget and the sill values are changed at different directions.

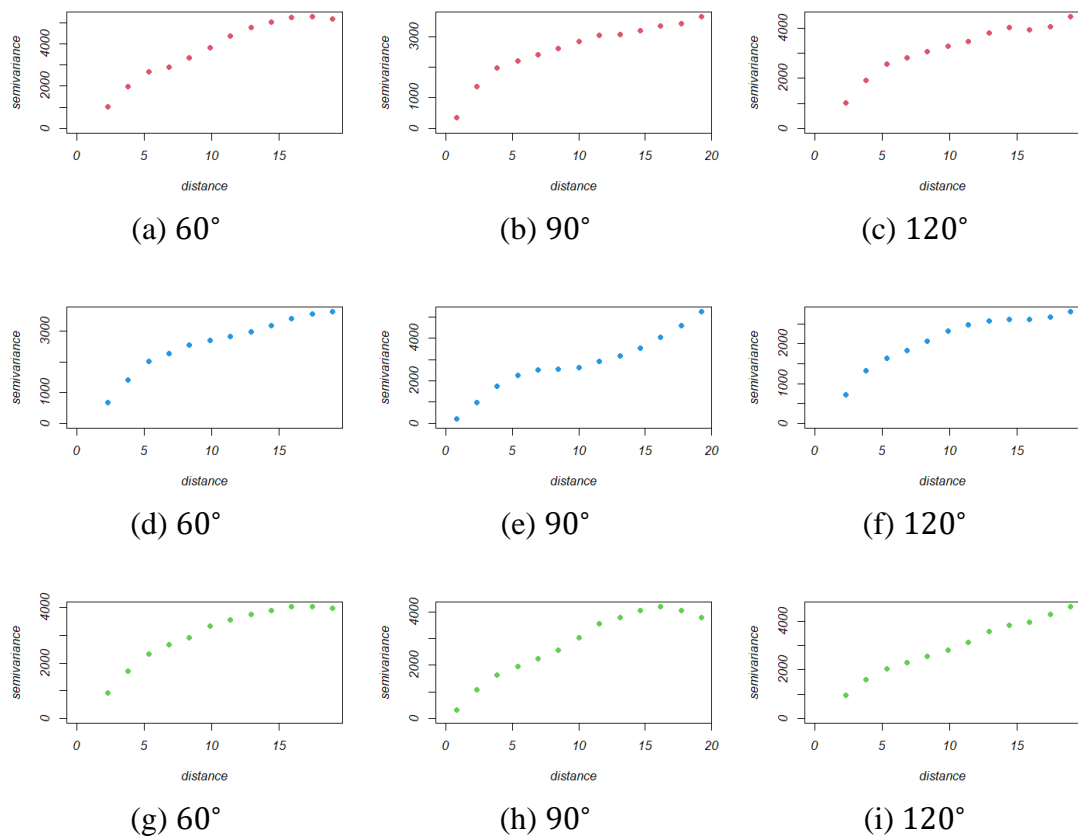


Figure 3.11: Panels (a) - (c) shows directional variogram for data of slice 10, panels (d) - (f) shows directional variogram for data of slice 11, and panels (g) - (i) shows directional variogram for data of slice 12

3.2.3 Model selection

Fig. 3.12 – 3.14, show different variogram models fitted for the empirical variograms in Fig. 3.4b, 3.4d, and 3.4f. The best variogram model is chosen by the cross validation in kriging. We use $K = 6, 5,$ and 6 folds for model selection in data image of slices 10, 11 and 12 respectively. In each fold we remove 317, 361 and 174 voxel for estimation the fitted model of slices 10, 11 and 12 respectively [28].

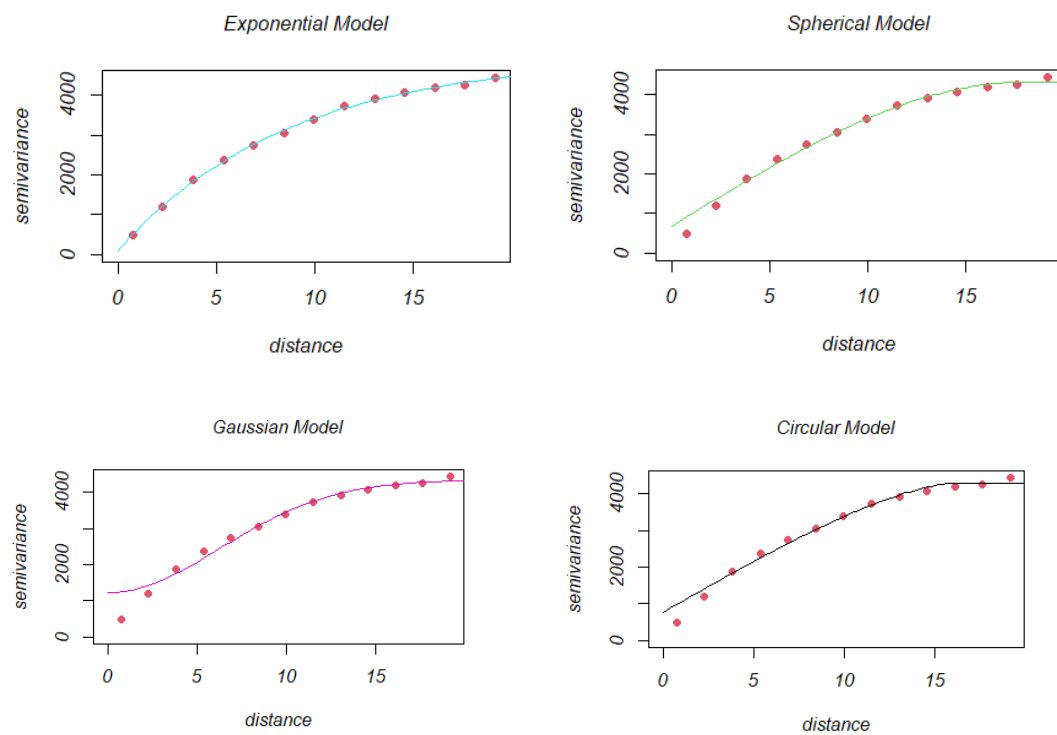


Figure 3.12: Exponential, spherical, Gaussian, and circular models are fitted (solid line) to the empirical variograms (dotted line) in Fig. 3.4b

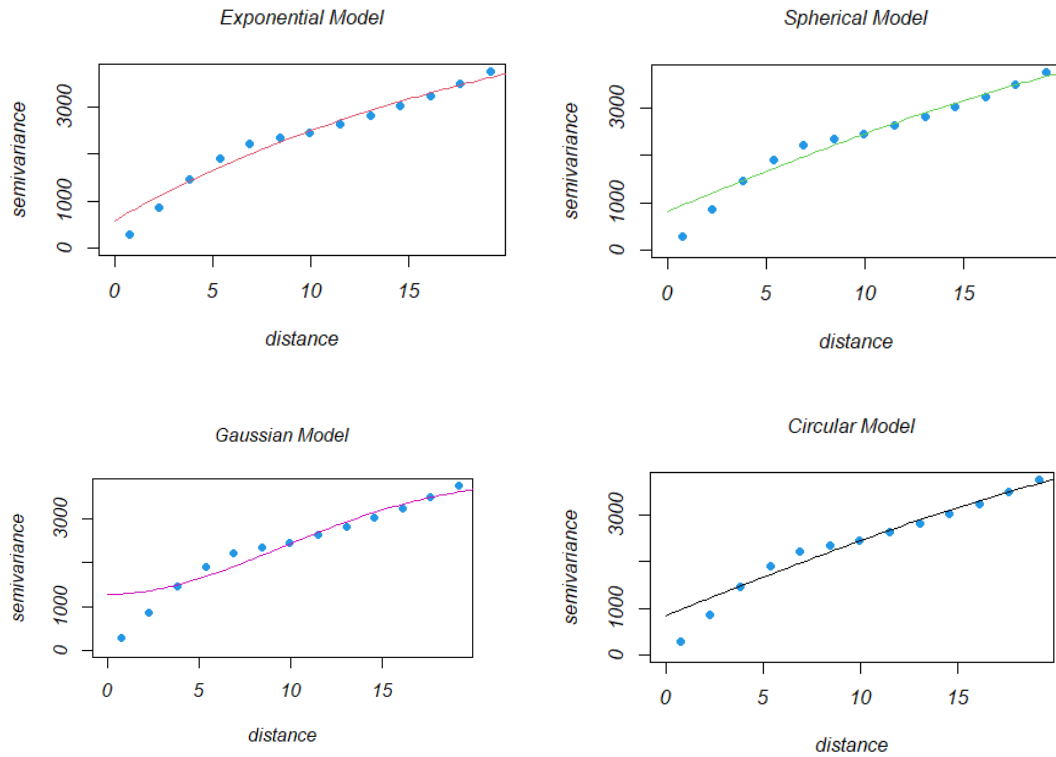


Figure 3.13: Exponential, spherical, Gaussian, and circular models are fitted (solid line) to the empirical variograms (dotted line) in Fig. 3.4d

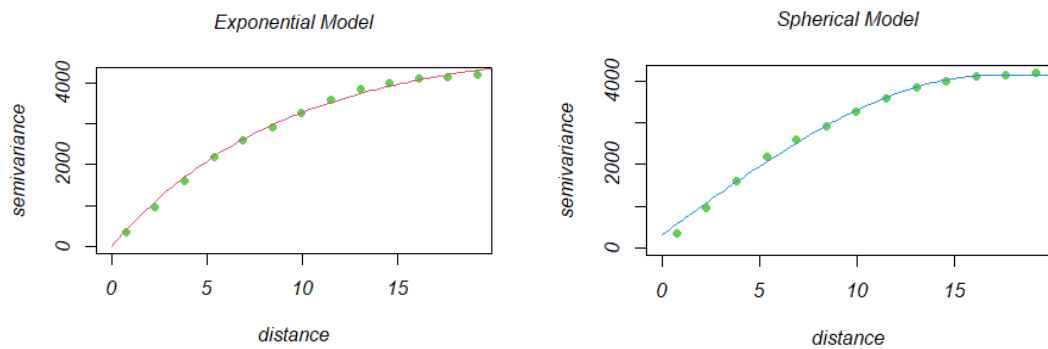


Figure 3.14: Exponential and spherical models are fitted (solid line) to the empirical variograms (dotted line) in Fig. 3.4f

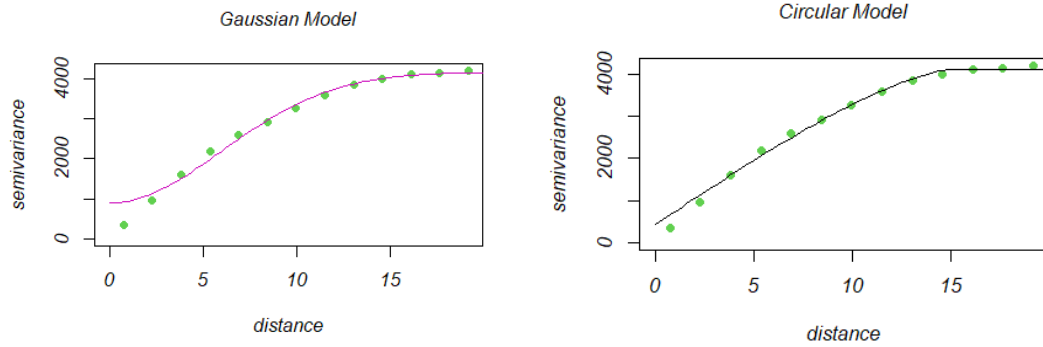


Figure 3.14: Gaussian, and circular models are fitted (solid line) to the empirical variograms (dotted line) in Fig. 3.4f

The MSDR in 3.1 is calculated and the best model will be the one which has MSDR value is the closest to 1. Table 3.3 shows the MSDR values for the variogram models approach in Fig. 3.12. The closest MSDR value to 1 is attained by the exponential model. Thus, the exponential model is the best variogram model approach for the empirical variogram in Fig. 3.4b and the estimated parameters for the sill, range and nugget are **4851.91**, **8.62** , and **91.95** respectively. As shown in table 3.4 the closest MSDR value to 1 is attained by the exponential model too. Therefore, the exponential model is the best variogram model approach for the empirical variogram in Fig. 3.4d and the estimated parameters for the sill, range and nugget are **5270.38**, **22.16** and **582.84** respectively.

Table 3.3: MSDR of the variogram models approach in 3.12

Variogram model	MSDR
Exponential Model	0.996
Spherical model	1.212
Circular model	1.733
Gaussian model	2.327

Table 3.4: MSDR of the variogram models approach in 3.13

Variogram Model	MSDR
Exponential model	0.976
Spherical model	1.249
Gaussian model	1.796
Circular model	1.722

Table 3.5 shows that the best variogram model approach for the empirical variogram in Fig. 3.4f is the Gaussian model with parameters estimate 3273.96 for the sill, 8.44 for the range and 895.63 for the nugget component.

Table 3.5: MSDR of the variogram models approach in 3.14

Variogram Model	MSDR
Exponential model	0.42282
Spherical model	0.5128
Gaussian model	1.047166
Circular model	0.78165

Tables 3.6 – 3.8 show the MSDR values for different directional variogram approach for angles 60°, 90°, and 120°. The exponential model is the best variogram model approach for the empirical variogram in Fig. 3.11a – 3.11f. On the other hand,

the best variogram model approach for the empirical variograms in Fig. 3.11g is the circular model and Gaussian model for Fig. 3.11h and 3.11i. The estimated parameters for these models are given in Table 3.9.

Table 3.6: MSDR of variogram models approach in figures 3, 4, and 5

Variogram model	60°	90°	120°
Circular model	1.428	1.842	1.690
Spherical model	1.126	1.219	1.201
Exponential model	0.941	1.074	0.978
Gaussian model	2.063	3.536	1.695

Table 3.7: MSDR of variogram models approach in figures 6, 7, and 8

Variogram model	60°	90°	120°
Circular model	2.042	2.158	1.859
Spherical model	1.197	1.432	1.327
Exponential model	0.920	1.211	0.951
Gaussian model	1.370	1.949	1.572

Table 3.8: MSDR of variogram models approach in figures 9, 10 and 11

Variogram model	60°	90°	120°
Circular model	0.680	0.765	0.555
Spherical model	0.443	0.509	0.467
Exponential model	0.383	0.429	0.423
Gaussian model	0.656	0.842	0.864

Table 3.9: The estimated parameters for the fitted directional variogram models in tables 3.6, 3.7, and 3.8

Slice 10				
Fitted Variogram model	Angle	Nugget	Sill	Range
Exponential model	60°	0.00	6644.13	10.98
Exponential model	90°	199.62	3401.10	76.30
Exponential model	120°	92.27	4629.21	8.10
Slice 11				
Fitted Variogram model	Angle	Nugget	Sill	Range
Exponential model	60°	0.00	4113.82	9.13
Exponential model	90°	0.00	2875.52	7.55
Exponential model	120°	0.00	2938.17	6.63
Slice 12				
Fitted Variogram model	Angle	Nugget	Sill	Range
Circular model	60°	480.37	3495.13	14.20
Gaussian model	90°	691.60	3400.48	8.52
Gaussian model	120°	1260.02	3696.51	13.15

3.3 Bootstrap sampling for estimating variogram parameters

In this section we will use a collection of bootstrap sampling techniques to estimate the variogram values and variogram parameters ([11], [13], [33]). Table 3.10 shows the original variogram values of the image data of interest region in slices 10, 11 and 12. To estimate the variogram parameters by using the bootstrap sampling technique we perform the bootstrap by two methods, the first one is based on the variogram cloud, we sample with replacement from each lag of the variogram cloud that is calculated by formula (3.2), from the average of the selected pairs in each lag we create a new variogram. The second method is based on errors obtained from the fitted model of the variogram [9], we sample with replacement from $\varepsilon^* = \varepsilon - \bar{\varepsilon}$. A new

variogram will be defined as $\gamma^*(h) = \gamma(h) + \varepsilon^*$, where $\gamma(h)$ is the fitted model. Fig. 3.15 shows the original variogram values and the variogram of each bootstrap performed by the aforementioned methods. The bootstrap variogram values based on variogram cloud clustered around the original variogram values (see Fig. 3.15b, 3.15d, and 3.15f). However, The bootstrap variogram values based on on errors obtained from the fitted model of the variogram are far from the original variogram values (see Fig. 3.15a, 3.15c, and 3.15e). Therefore, the first method gives a better estimate for variogram parameters than the second method (see Fig. 3.16 and 3.17).

Table 3.10: Original variogram

Distance	$\hat{\gamma}(h)$ -slice 10	$\hat{\gamma}(h)$ -slice 11	$\hat{\gamma}(h)$ -slice 12
0.7663407	477.9849	294.0081	347.1577
2.2990222	1210.5489	848.446	963.5470
3.8317036	1869.8618	1450.2033	1606.363
5.36438518	2382.385	1913.6317	2181.6728
6.8970665	2742.6729	2205.3724	2584.3717
8.429748	3042.5699	2340.8942	2918.2092
9.9624294	3377.9585	2458.187	3256.0743
11.4951109	3714.2686	2627.8597	3592.1196
13.0277923	3923.8582	2826.7985	3850.6353
14.5604738	4057.3051	3026.1601	4010.6137
16.0931552	4201.928	3241.8101	4103.3627
17.6258367	4265.2613	3500.48	4136.6555
19.1585181	4437.254	3760.6256	4202.7866

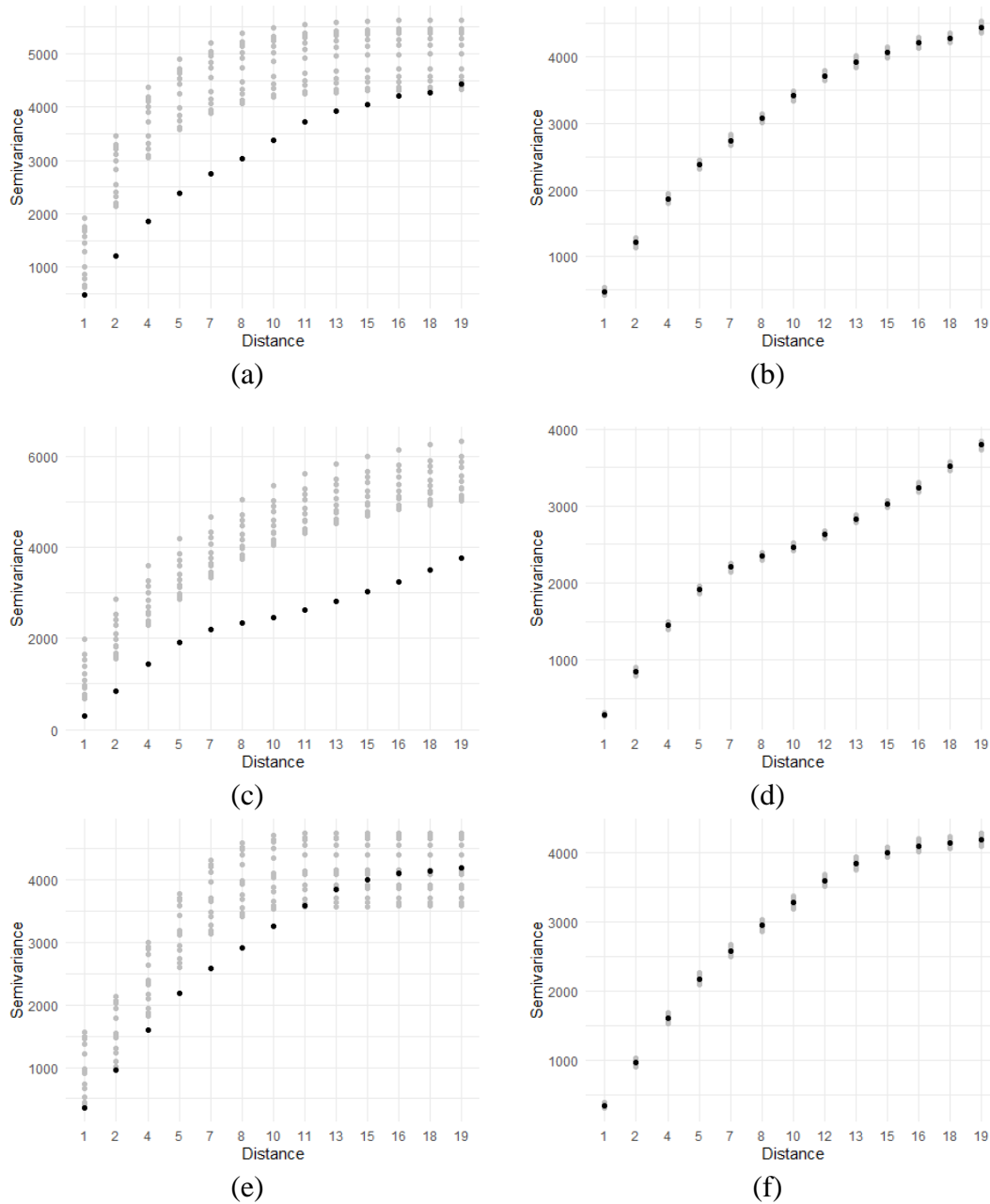


Figure 3.15: Panels (a), (c), and (d) show the original variogram and the variogram of each bootstrap performed by variogram bootstrap for the slices 10, 11, and 12 respectively. Panels (b), (d), and (f) are the original variogram and the variogram of each bootstrap based on variogram cloud.

Tables 3.11 and 3.12 show the 95% confidence interval for the nugget, sill and range estimated values from bootstrap techniques discussed before. These results shows how

the confidence intervals of cloud bootstrap method are tightly comparable with variogram bootstrap method.

Table 11: 95% confidence interval for the variogram parameters estimated by the cloud bootstrap method.

Slice 10			
Parameter	Lower	Estimate	Upper
Nugget	9.1364	91.9534	139.6389
Sill	4852.5042	4943.8684	5006.4070
Range	8.1207	8.6176	8.8819
Slice 11			
Parameter	Lower	Estimate	Upper
Nugget	554.1299	582.8352	646.6061
Sill	5656.3107	5853.2071	6757.7237
Range	20.7232	22.1562	27.9232
Slice 12			
Parameter	Lower	Estimate	Upper
Nugget	839.0443	895.6139	924.1837
Sill	4125.5378	4169.5831	4196.9068
Range	8.1561	8.4401	8.5385

Table 3.12: 95% confidence interval for the variogram parameters estimated by the variogram bootstrap method.

Slice 10			
Parameter	Lower	Estimate	Upper
Nugget	0.0000	91.9534	2142.3364
Sill	4593.9907	4943.8684	5700.5712
Range	1.8658	8.6176	7.8430
Slice 11			

Parameter	Lower	Estimate	Upper
Nugget	0.0000	582.8352	1777.2206
Sill	5255.9936	5853.2071	9548.2481
Range	4.7487	22.1562	24.9446

Slice 12

Parameter	Lower	Estimate	Upper
Nugget	57.6628	895.6139	1730.7885
Sill	3885.4564	4169.5831	4521.0533
Range	3.5628	8.4401	6.9764

Fig. 3.16a, 3.16c, and 3.16e show the estimate bootstrap sill values by using the bootstrap variogram based on variogram cloud method for slices 10, 11, and 12 respectively. The red solid line represents the original sill values and the green solid lines represent the upper and lower confidence interval bounds of the 1000 bootstrap sill values. Fig. 3.16b, 3.16d, and 3.16f show the correspondent estimate bootstrap sill values based on error from the fitted model of the variogram. As we can see from Fig. 3.16b and 3.16d the values of the bootstrap sill are greater than the values in Fig. 3.16a and 3.16c, this is because the bootstrap variogram values are far from the original values.

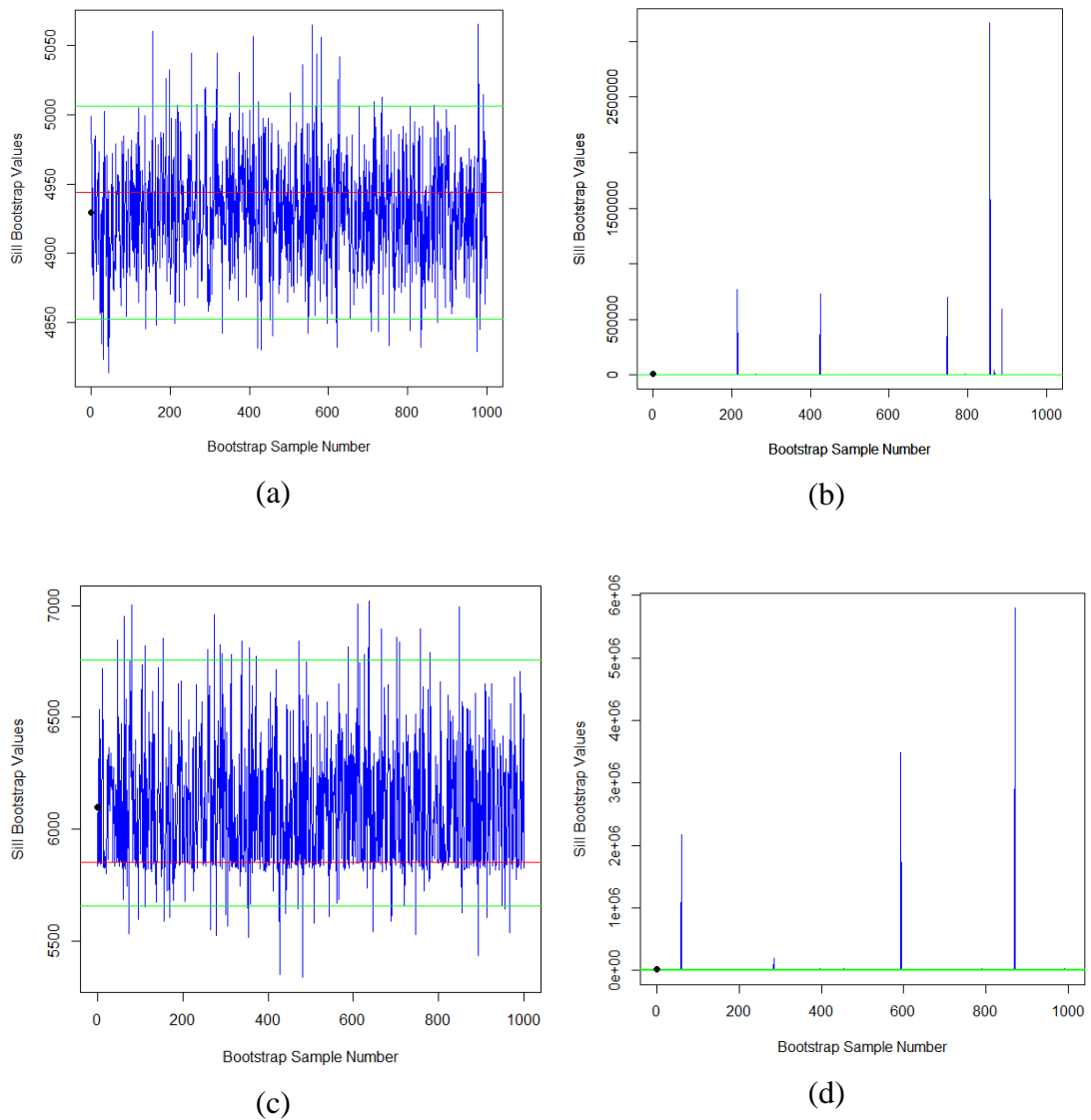


Figure 3.16: Panels (a) and (c) shows the original sill and estimated sill values for each bootstrap by using bootstrap of the variogram cloud while panels (b) and (d) are from bootstrap based on error from the fitted model of the variogram. (- original sill, - confidence interval bounds, • average of sill bootstrap values).

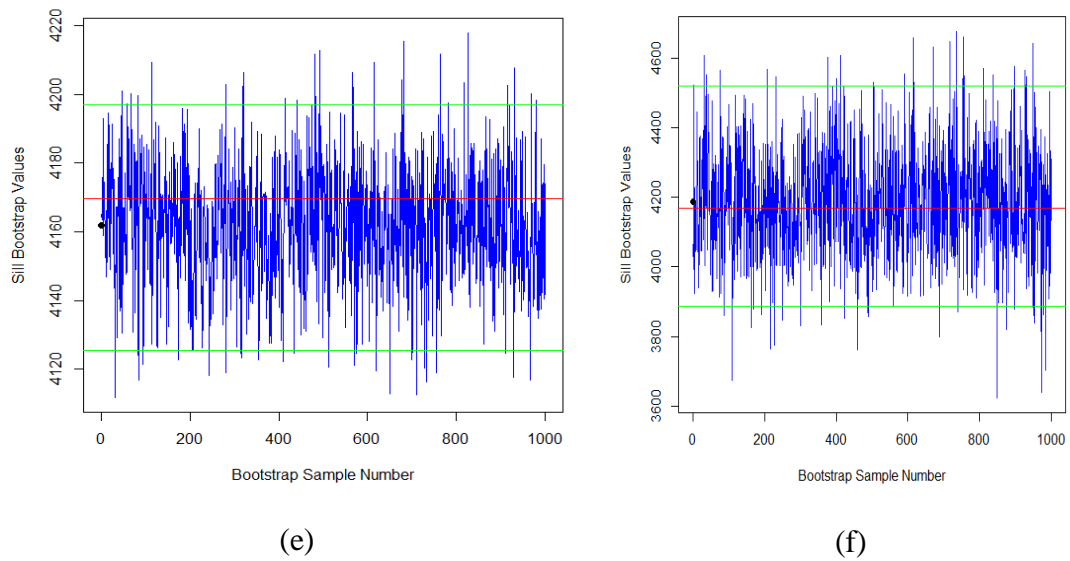
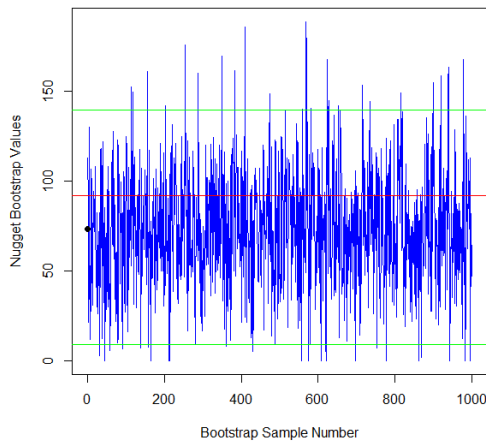
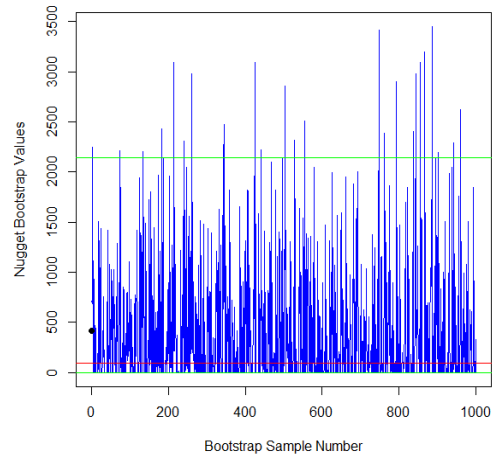


Figure 3.16: Panels (e) and (f) shows the original sill and estimated sill values for each bootstrap by using bootstrap of the variogram cloud and bootstrap based on error from the fitted model of the variogram respectively. (- original sill, - confidence interval bounds, • average of sill bootstrap values)

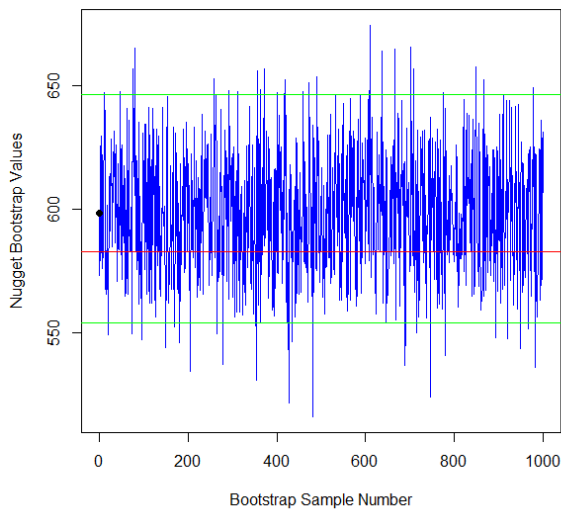
Fig. 3.17a, 3.17c, and 3.17e show the nugget values of the 1000 variogram bootstrap performed based on variogram cloud for slices 10, 11, and 12 respectively. These figures show how the estimated nugget values are closer to the original value than these performed based on errors obtained from the fitted model of the variogram (see Fig. 3.17b, 3.17d, and 3.17f).



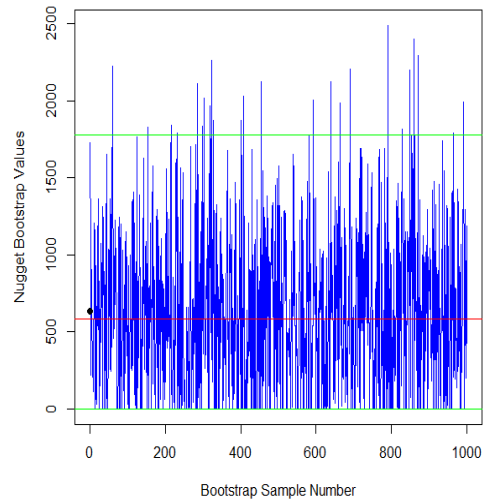
(a)



(b)

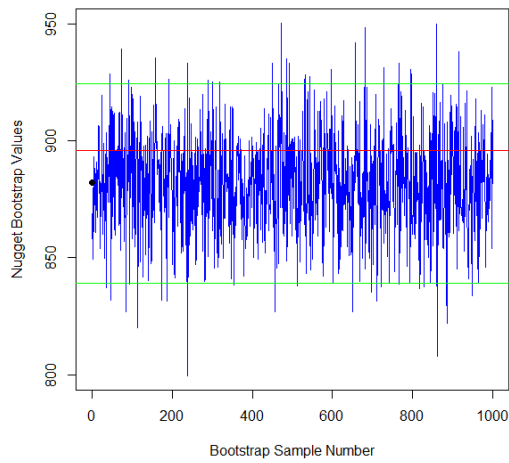


(c)

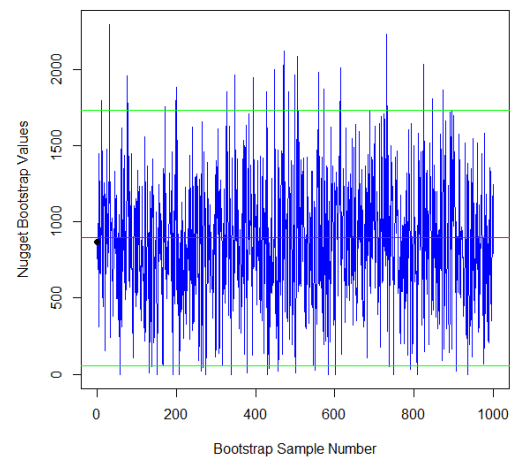


(d)

Figure 3.17: Panels (a) and (c) shows the original nugget and estimated nugget values for each bootstrap by using bootstrap of the variogram cloud while panels (b) and (d) are from bootstrap based on error from the fitted model of the variogram. (- original nugget, - confidence interval bounds, • average of nugget bootstrap values)



(e)



(f)

Figure 3.17: Panels (e) and (f) shows the original nugget and estimated nugget values for each bootstrap by using bootstrap of the variogram cloud and bootstrap based on error from the fitted model of the variogram respectively. (- original nugget, - confidence interval bounds, • average of nugget bootstrap values)

CHAPTER 4: CONCLUSION AND FUTURE WORK

In this work we applied the variogram and kriging methods to study the spatial correlation between the brain tumor voxels in three slices of MRI images (see Fig. 3.2). After masking the brain process and checking the validation of the stationary assumption we perform statistical analysis to calculate the empirical variogram and we used the k -fold cross validation to choose the best variogram model. Finally we found that the exponential variogram model is the best model for the spatial correlation in slices 10 and 11 and the gaussian model in slice 12. Also, we apply bootstrap sampling technique to estimate the variogram values and parameters of the fitted models.

This work can be extended to spatiotemporal analysis into two ways. First, by using the functional magnetic resonance imaging (fMRI) to study the brain activity of the tumor region during a time period. Also, in case of availability the MRI images for a patient in more than one visit so we can predict the growth of brain for future.

In this work we performed the variogram analysis for each slice of brain separately, where each slice represents a matrix. This work can be extended to be in 3 dimensions where is third dimension represents the number of slice (see appendix C).

REFERENCES

- [1] Introduction to Neurohacking In R - Home — Coursera.
- [2] Sudipto Banerjee, Bradley P Carlin, and Alan E Gelfand. Hierarchical modeling and analysis for spatial data. CRC press, 2014.
- [3] Dimitri P Bertsekas. Constrained optimization and Lagrange multiplier methods. Academic press, 2014.
- [4] Geoff Bohling. Introduction to geostatistics and variogram analysis. Kansas geological survey, 1(10):1–20, 2005.
- [5] F Dubois Bowman. Spatiotemporal models for region of interest analyses of Functional neuroimaging data. Journal of the American Statistical Association, 102(478):442–453, 2007.
- [6] Paul T Callaghan. Principles of nuclear magnetic resonance microscopy. Oxford University Press on Demand, 1993.
- [7] Wenjie Chen, Haipeng Shen, and Young K Truong. Spatio-temporal modeling for fmri data. In Time Series Analysis and Forecasting, pages 293–311. Springer, 2016.
- [8] R Corstanje, S Grunwald, and RM Lark. Inferences from fluctuations in the local variogram about the assumption of stationarity in the variance. Geoderma, 143(1-2):123–132, 2008.
- [9] Anthony Christopher Davison and David Victor Hinkley. Bootstrap methods and their application. Number 1. Cambridge university press, 1997.
- [10] Tingting Dong, Qiuping Huang, Shucui Huang, Jiang Xin, Qiaolan Jia, Yang Gao, Hongxian Shen, Yan Tang, and Hao Zhang. Identification of methamphetamine abstainers by resting-state functional magnetic resonance imaging. Frontiers in psychology, 12, 2021.

- [11] Bradley Efron and Robert Tibshirani. The bootstrap method for assessing statistical accuracy. *Behaviormetrika*, 12(17):1–35, 1985.
- [12] Xavier Emery. Simple and ordinary multigaussian kriging for estimating recoverable reserves. *Mathematical Geology*, 37(3):295–319, 2005.
- [13] Pilar Garc'ia-Soid'an, Raquel Menezes, and Oscar Rubi~nos. Bootstrap approaches for spatial data. *Stochastic environmental research and risk assessment*, 28(5):1207–1219, 2014.
- [14] Diego Giuliani, Maria Michela Dickson, Giuseppe Espa, and Flavio Santi. Modelling and predicting the spatio-temporal spread of covid-19 in italy. *BMC infectious diseases*, 20(1):1–10, 2020.
- [15] Feng Gui and Lin Qi Wei. Application of variogram function in image analysis. In *Proceedings 7th International Conference on Signal Processing*, 2004. *Proceedings. ICSP'04. 2004.*, volume 2, pages 1099–1102. IEEE, 2004.
- [16] MA Gurskaya, J Lange, VV Kukarskih, A Buras, and M Wilmking. Stationarity of climate-growth response is only marginally influenced by the soil moisture regime in western siberia. *Dendrochronologia*, 69:125873, 2021.
- [17] Timothy C Haas. Lognormal and moving window methods of estimating acid deposition. *Journal of the American Statistical Association*, 85(412):950–963, 1990.
- [18] Chunfeng Huang, Haimeng Zhang, and Scott M Robeson. On the validity of commonly used covariance and variogram functions on the sphere. *Mathematical Geosciences*, 43(6):721–733, 2011.
- [19] Scott A Huettel, Allen W Song, Gregory McCarthy, et al. *Functional magnetic resonance imaging*, volume 1. Sinauer Associates Sunderland, MA, 2004.
- [20] Edward H Isaaks and Mohan R Srivastava. *Applied geostatistics*. Number

551.72 ISA. 1989.

- [21] EH Isaaks and RM Srivastava. An introduction to applied geostatistics, 1989. New York, USA: Oxford University Press. Jones DR, A taxonomy of global optimization methods based on response surfaces. *Journal of Global Optimization*, 23:345–383, 2001.
- [22] Mark Jenkinson and Michael Chappell. Introduction to neuroimaging analysis. Oxford University Press, 2018.
- [23] Kota Katanoda, Yasumasa Matsuda, and Morihiro Sugishita. A spatio-temporal regression model for the analysis of functional mri data. *NeuroImage*, 17(3):1415–1428, 2002.
- [24] R. M. Lark. Estimating variograms of soil properties by the method-of-moments and maximum likelihood. *European Journal of Soil Science*, 51(4):717–728, 2000.
- [25] Esam Mahdi, Ali H Abuzaid, and Abdu Atta. Empirical variogram for achieving the best valid variogram. *Communications for Statistical Applications and Methods*, 27(5):547–568, 2020.
- [26] H Manto. Modelling of geometric anisotropic spatial variation. *Mathematical Modelling and Analysis*, pages 361–366, 2005.
- [27] Robert Marschallinger, Carmen Tur, Hannes Marschallinger, and Johann Sellner. A r-script for generating multiple sclerosis lesion pattern discrimination plots. *Brain Sciences*, 11(1):90, 2021.
- [28] SMMatechik and MR Stytz. Using kriging to interpolate mri data. In *Proceedings of 16th Annual International Conference of the IEEE Engineering in Medicine and Biology Society*, volume 1, pages 576–577. IEEE, 1994.
- [29] Cressie NAC. Cressie nac statistics for spatial data. *Probab Math Statist*, 1993.

- [30] J Polzehl and K Tabelow. Magnetic resonance brain imaging: Modeling and data analysis. 2019.
- [31] Paulo J Ribeiro Jr, Peter J Diggle, Maintainer Paulo J Ribeiro Jr, and MASS Suggests. The geor package. R news, 1(2):14–18, 2007.
- [32] Oliver Schabenberger and Carol A Gotway. Statistical methods for spatial data analysis. CRC press, 2017.
- [33] Kesar Singh and Minge Xie. Bootstrap: a statistical method. Unpublished manuscript, Rutgers University, USA. Retrieved from <http://www.stat.rutgers.edu/home/mxie/RCPapers/bootstrap.pdf>, pages 1–14, 2008.
- [34] Christina Stoehr, John AD Aston, and Claudia Kirch. Detecting changes in the covariance structure of functional time series with application to fmri data. *Econometrics and Statistics*, 18:44–62, 2021.
- [35] Richard Webster and Margaret A. Oliver. Geostatistics for environmental scientists. *Statistics in Practice*, 2007.
- [36] Richard Webster and Margaret A Oliver. Geostatistics for environmental scientists. John Wiley & Sons, 2007.
- [37] Brandon Whitcher, Volker J Schmid, and Andrew Thornton. Working with the dicom and nifti data standards in r. *Journal of Statistical Software*, 44(1):1–29, 2011.
- [38] Brandon Whitcher and Maintainer Brandon Whitcher. Package ‘oro.dicom’. 2015.
- [39] Jun Ye, Nicole A Lazar, and Yehua Li. Nonparametric variogram modeling with hole effect structure in analyzing the spatial characteristics of fmri data. *Journal of neuroscience methods*, 240:101–115, 2015.
- [40] Xian-Chuan Yu, Chen Yu, Xiao-Chun Cheng, Shao-Chun Zhong, and Ting

Zhang. Analyzing fmri data based on multi-resolution factorial kriging. In Proceedings of 2004 International Conference on Machine Learning and Cybernetics (IEEE Cat. No. 04EX826), volume 7, pages 4009–4014. IEEE, 2004.

- [41] Dale L Zimmerman and M Bridget Zimmerman. A comparison of spatial semivariogram estimators and corresponding ordinary kriging predictors. *Technometrics*, 33(1):77–91, 1991.

APPENDIX A: HISTOGRAM OF THE ESTIMATED PARAMETERS

The following figures show histograms of variogram parameters estimated by using bootstrap of the variogram cloud and from bootstrap based on error from the fitted model of the variogram. The vertical red lines are the upper and lower bound of the confidence intervals.

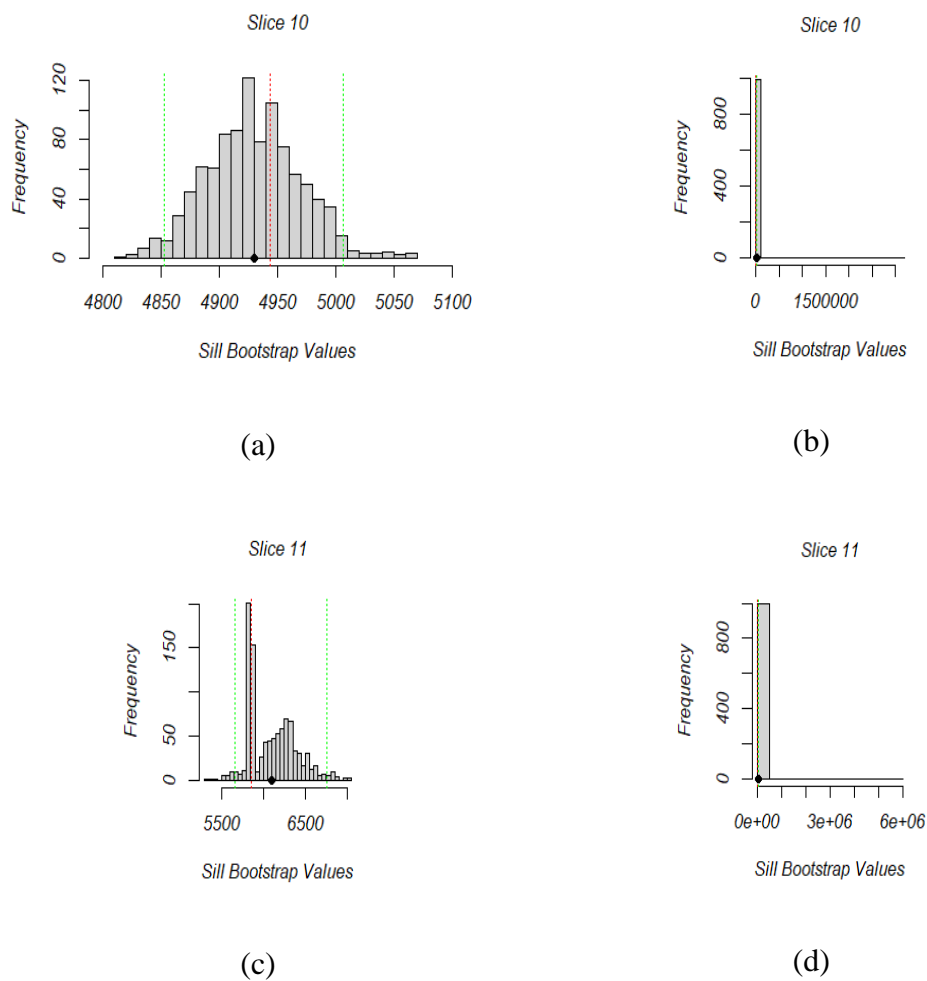
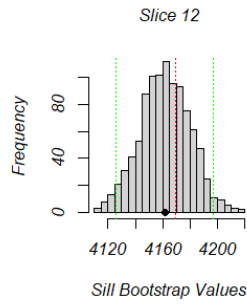
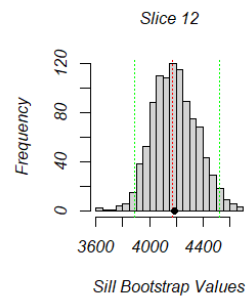


Figure 1: Panels (a) and (c) show a histogram of bootstrap sill values by using the bootstrap of the variogram cloud, while panels (b) and (d) are from bootstrap based on error from the fitted model of the variogram (- original sill, - confidence interval bounds, • average of sill bootstrap values)

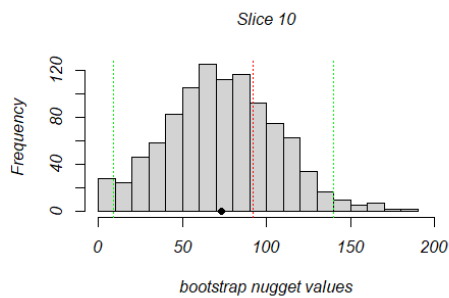


(e)

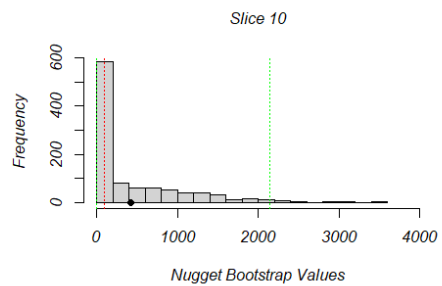


(f)

Figure 1: Panel (e) shows a histogram of bootstrap sill values by using the bootstrap of the variogram cloud, while panel (f) are from bootstrap based on error from the fitted model of the variogram (- original sill, - confidence interval bounds, • average of sill bootstrap values)

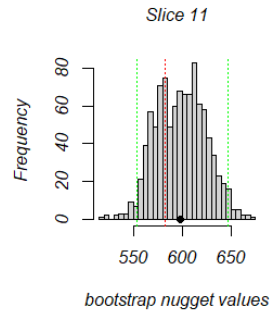


(a)

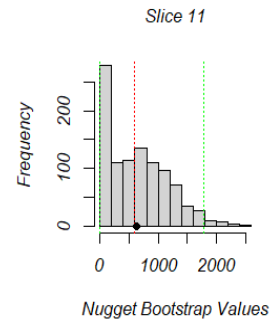


(b)

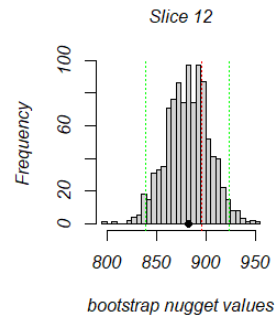
Figure 2: Panel (a) shows a histogram of bootstrap nugget values by using the bootstrap of the variogram cloud, while panel (b) are from bootstrap based on error from the fitted model of the variogram (- original nugget, - confidence interval bounds, • average of nugget bootstrap values)



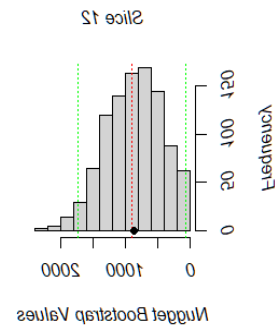
(a)



(b)



(c)



(d)

Figure 2: Panels (c) and (e) show a histogram of bootstrap nugget values by using the bootstrap of the variogram cloud, while panels (f) and (d) are from bootstrap based on error from the fitted model of the variogram (- original nugget, - confidence interval bounds, • average of nugget bootstrap values).

APPENDIX B: FITTED MODELS TO THE DIRECTIONAL EMPIRICAL MODELS

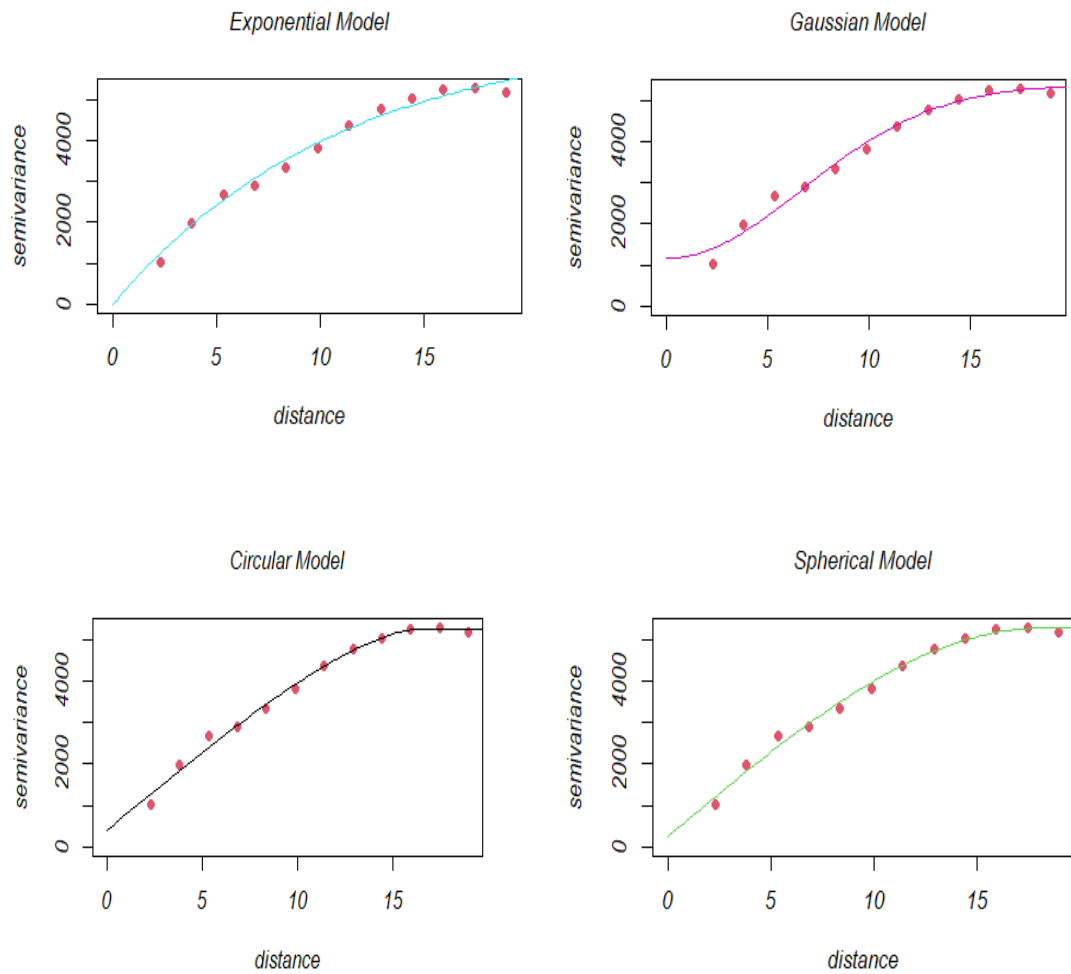


Figure 3: Exponential, Gaussian, circular, and spherical models are fitted (solid line) to the empirical variograms (dotted line) in Fig. 3.11a

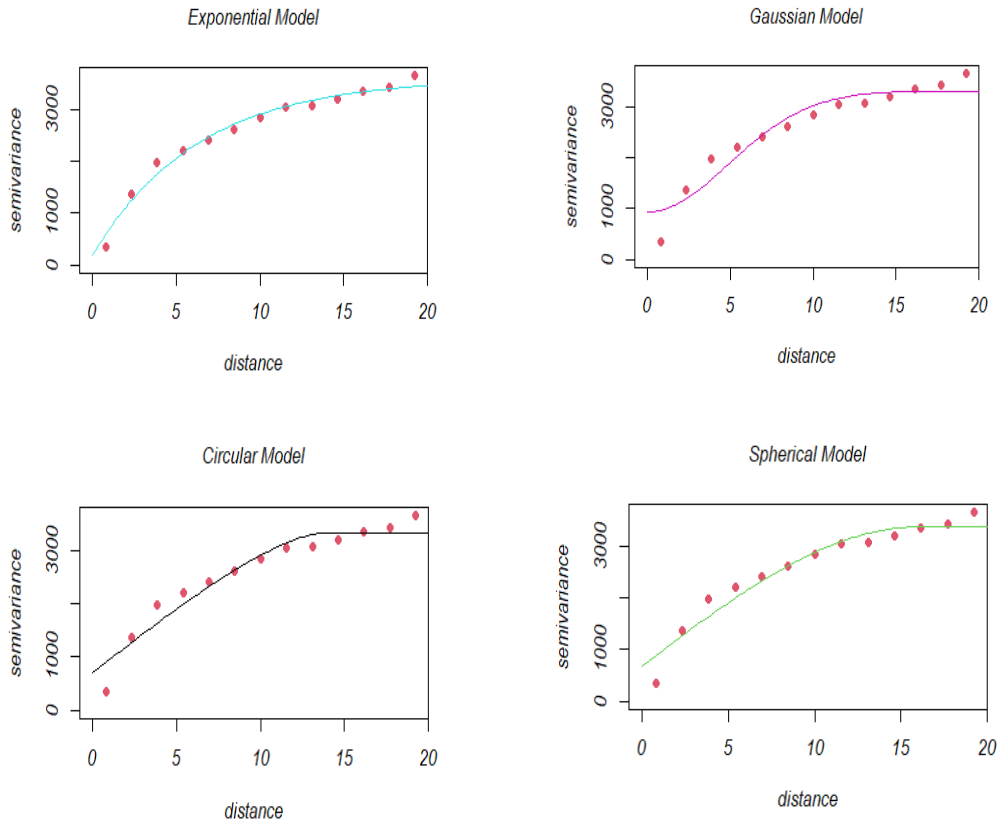


Figure 4: Exponential, Gaussian, circular, and spherical models are fitted (solid line) to the empirical variograms (dotted line) in Fig. 3.11b

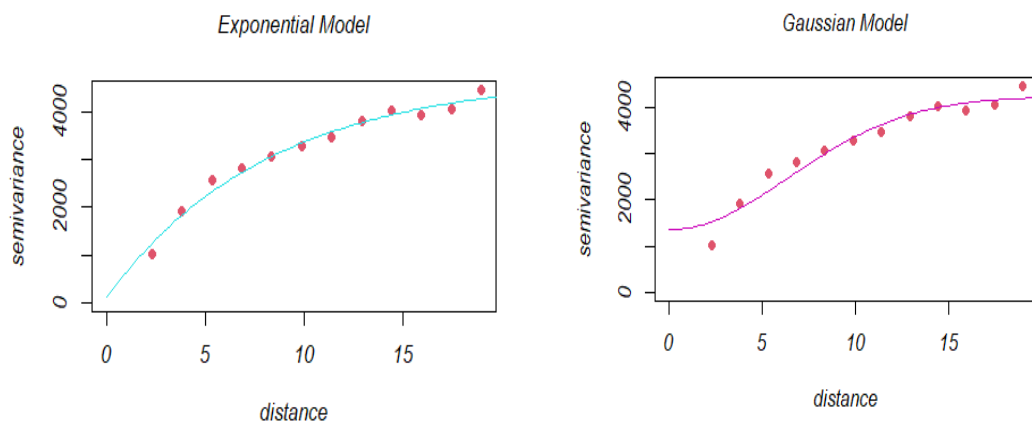


Figure 5: Exponential and Gaussian models are fitted (solid line) to the empirical variograms (dotted line) in Fig. 3.11c

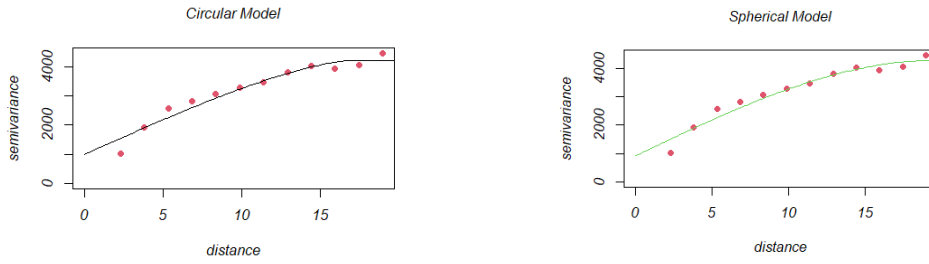


Figure 5: Circular and spherical models are fitted (solid line) to the empirical variograms (dotted line) in Fig. 3.11c

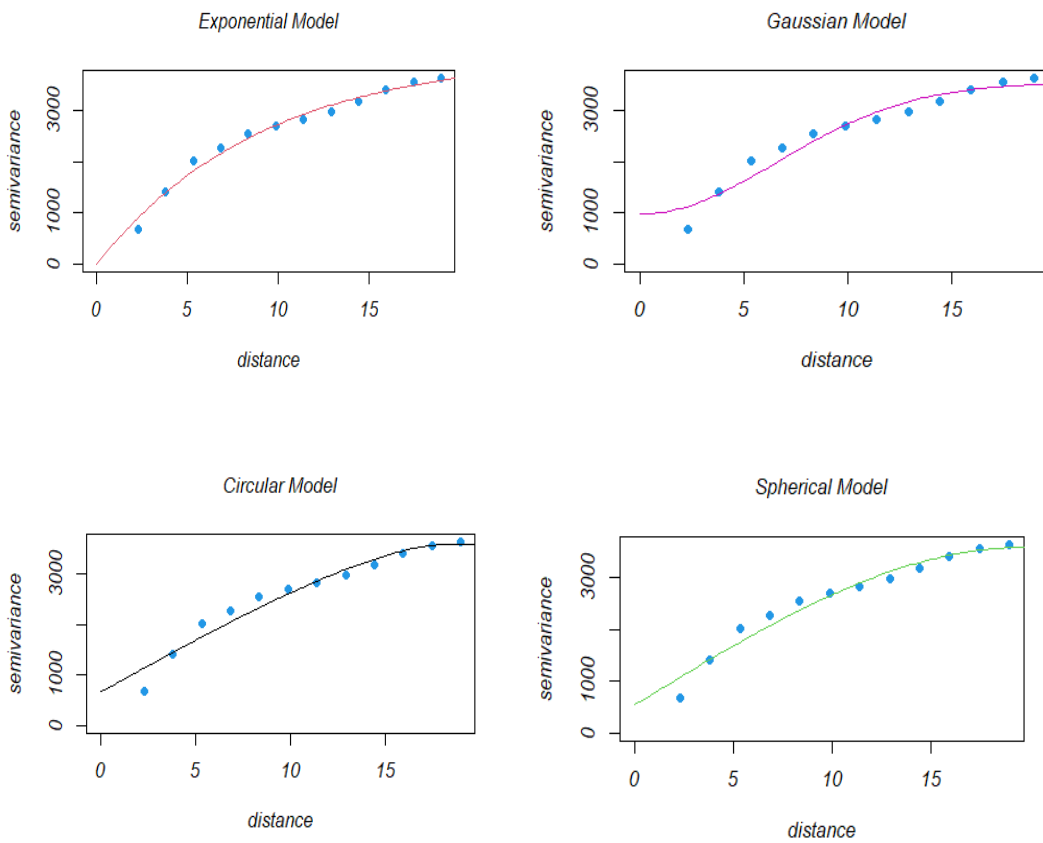


Figure 6: Exponential, Gaussian, circular, and spherical models are fitted (solid line) to the empirical variograms (dotted line) in Fig. 3.11d

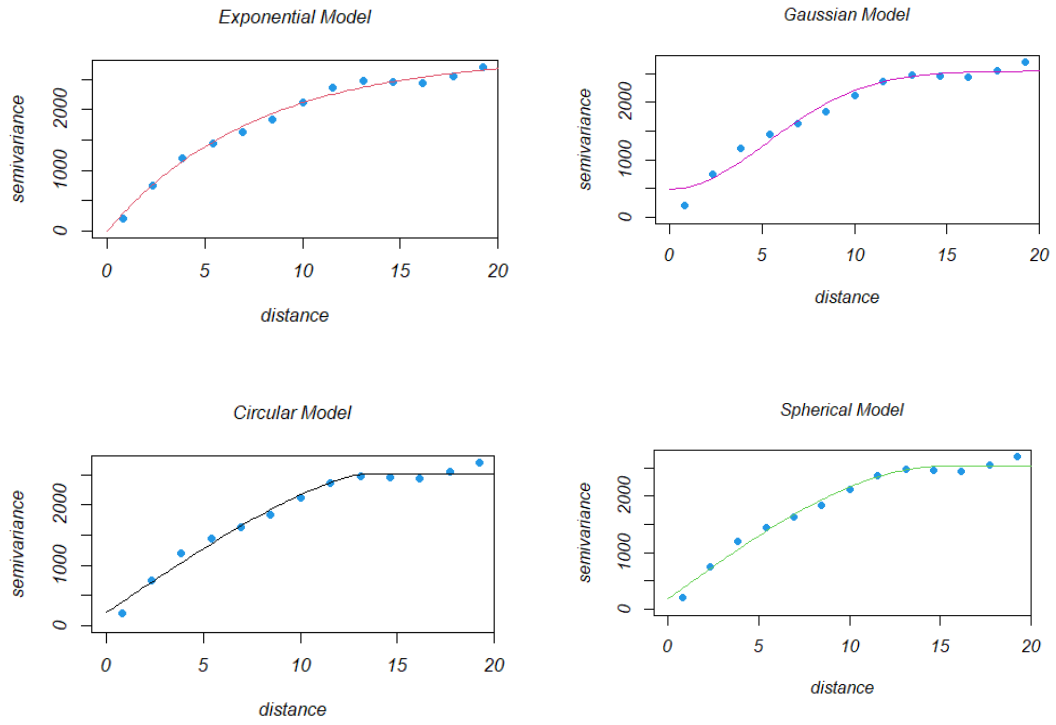


Figure 7: Exponential, Gaussian, circular, and spherical models are fitted (solid line) to the empirical variograms (dotted line) in Fig. 3.11e

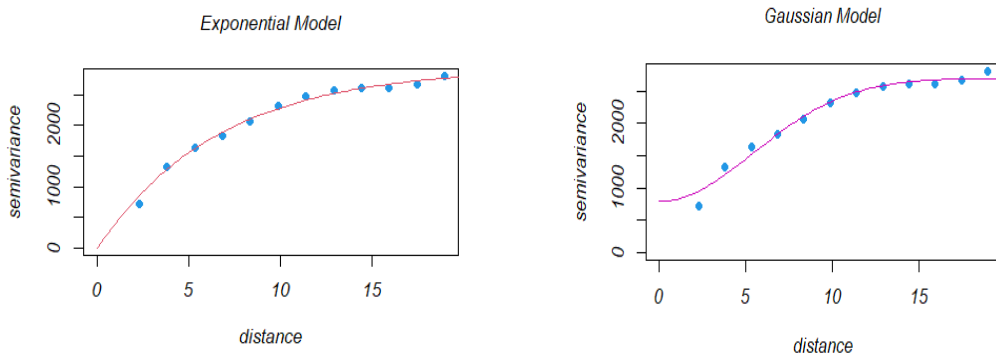


Figure 8: Exponential and Gaussian models are fitted (solid line) to the empirical variograms (dotted line) in Fig. 3.11f

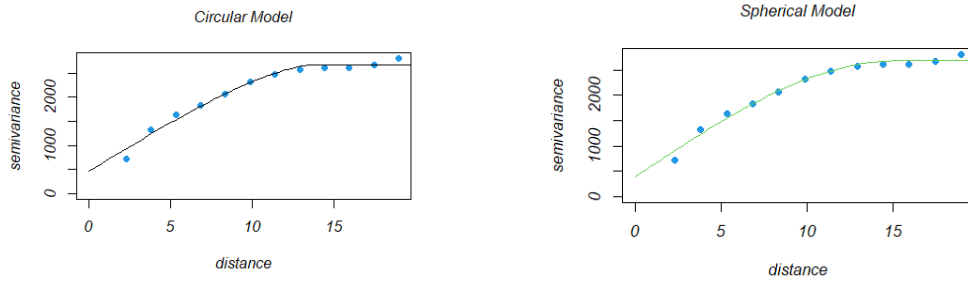


Figure 8: Circular, and spherical models are fitted (solid line) to the empirical variograms (dotted line) in Fig. 3.11f

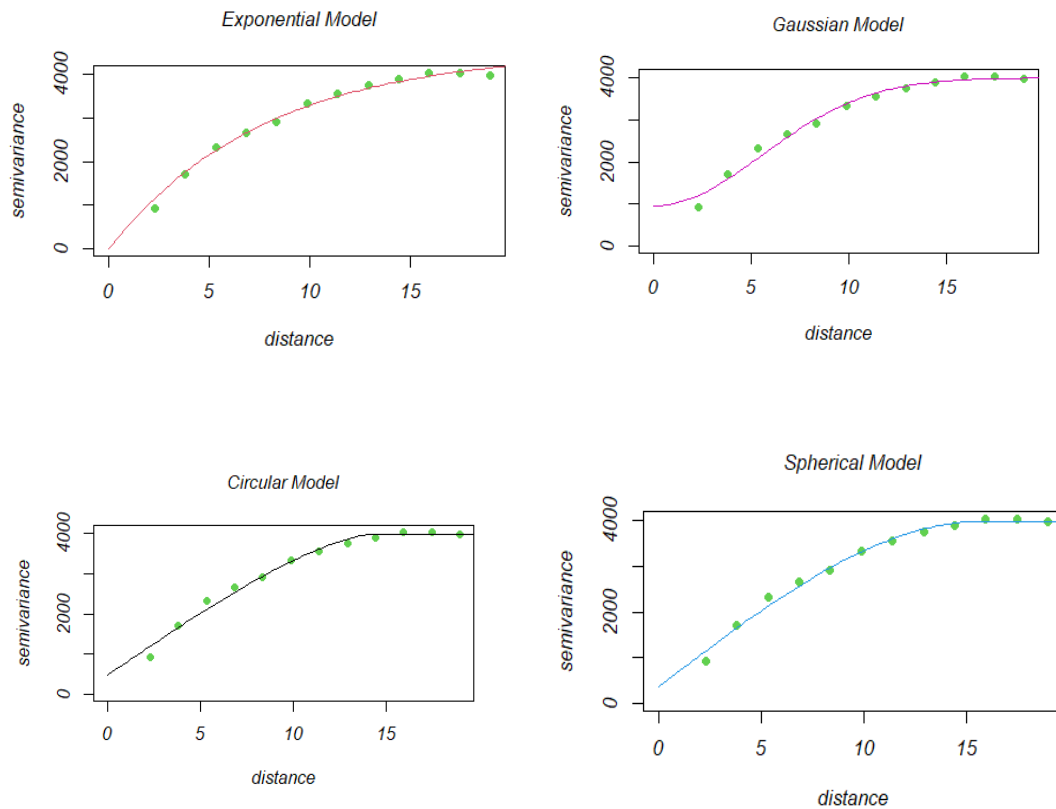


Figure 9: Exponential, Gaussian, circular, and spherical models are fitted (solid line) to the empirical variograms (dotted line) in Fig. 3.11g

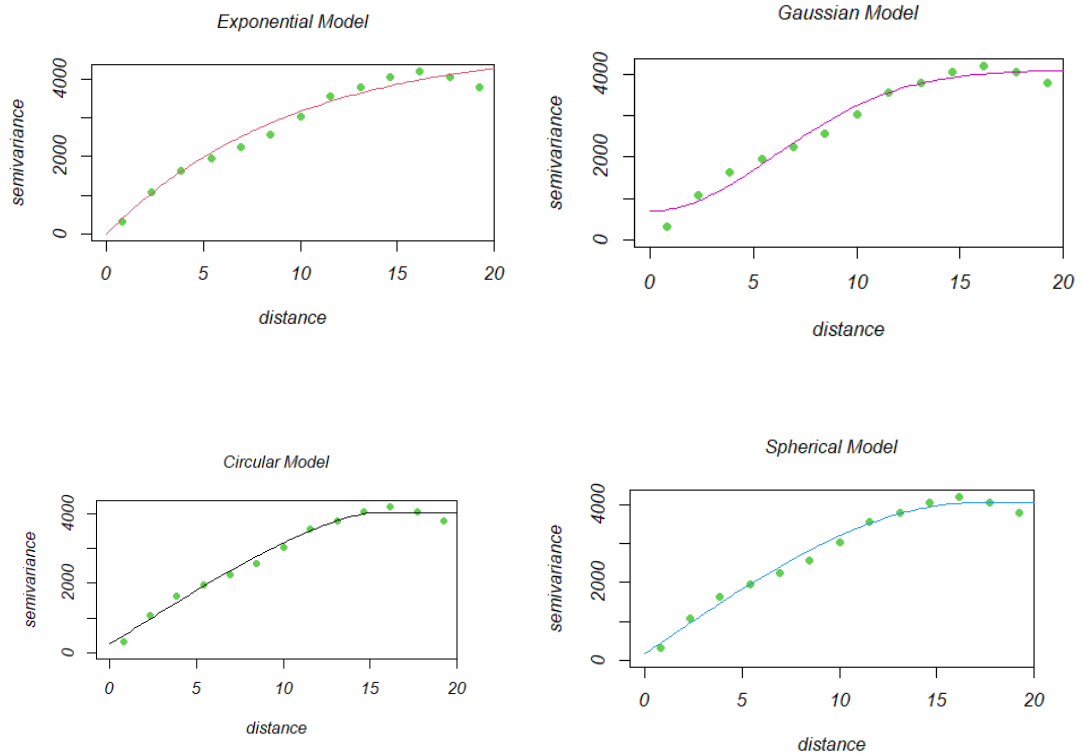


Figure 10: Exponential, Gaussian, circular, and spherical models are fitted (solid line) to the empirical variograms (dotted line) in Fig. 3.11h

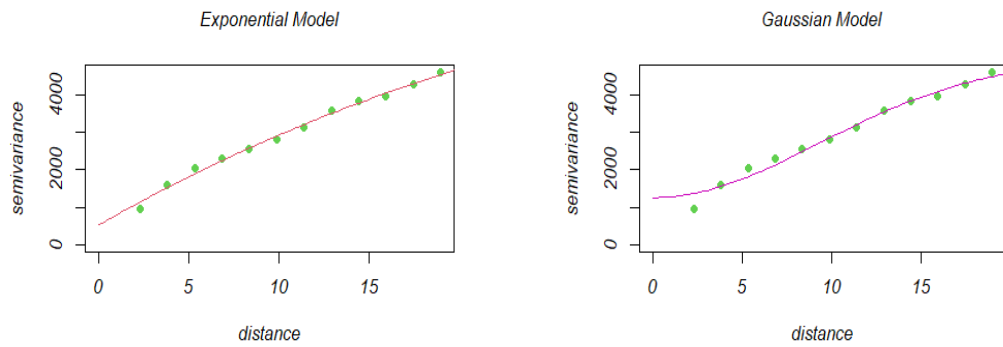


Figure 11: Exponential and Gaussian models are fitted (solid line) to the empirical variograms (dotted line) in Fig. 3.11i

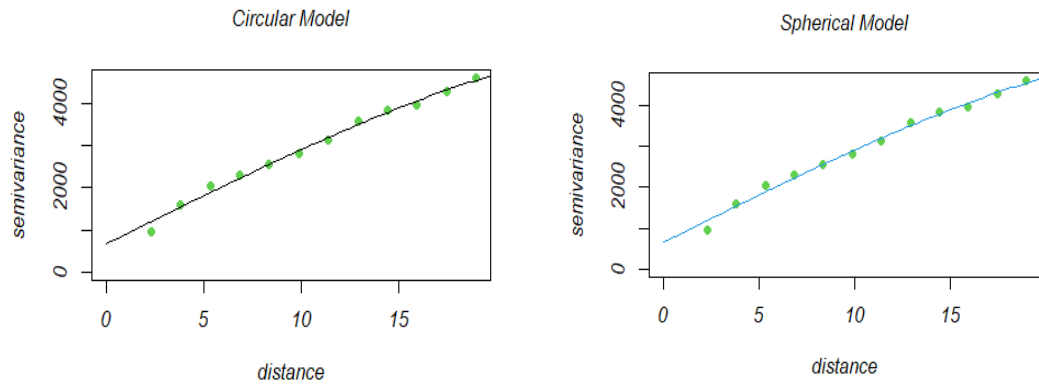
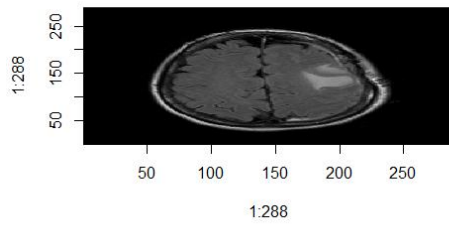
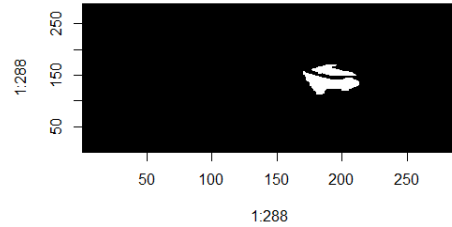


Figure 11: Circular, and spherical models are fitted (solid line) to the empirical variograms (dotted line) in Fig. 3.11i

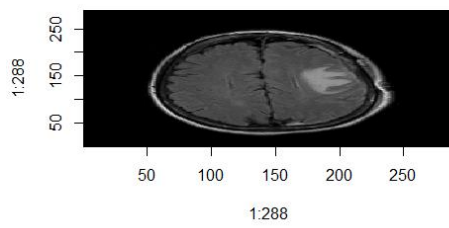
APPENDIX C: EMPIRICAL VARIOGRAM OF ALL SLICES



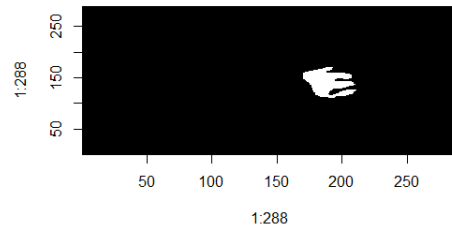
(a)



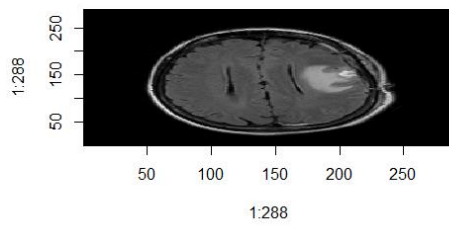
(b)



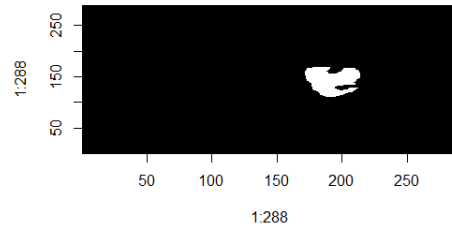
(c)



(d)



(e)



(f)

Figure 12: Panels (a), (c) and (e) show the MRI images for slices 7, 8 and 9 in figure 15 and panels (b), (d) and (f) represent the region of interest for these slices respectively.

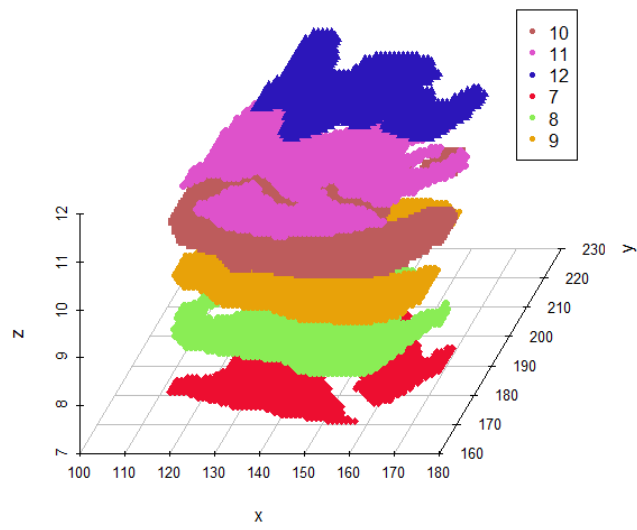


Figure 13: 3 dimension plot for the data in slices 7,8,9,10,11 and 12

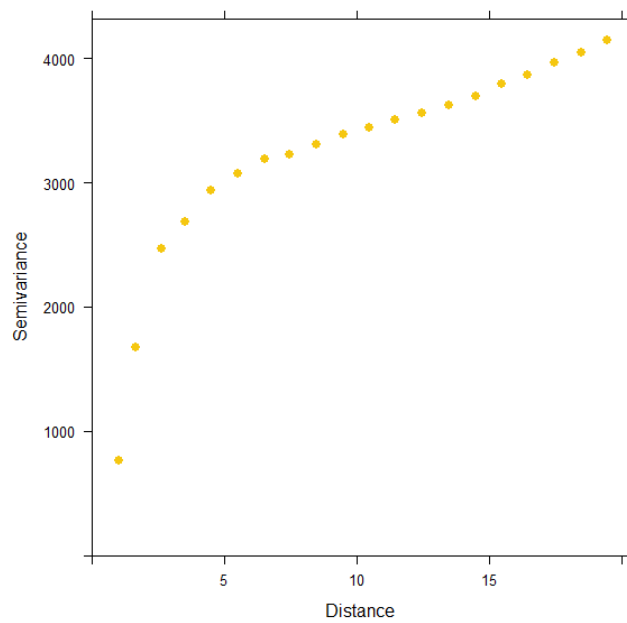


Figure 14: Empirical variogram for the data in slices 7, 8, 9, 10, 11, and 12